

**Ericksen number and Deborah number cascade predictions of a model for
liquid crystalline polymers for simple shear flow**

D. Harley Klein* and L. Gary Leal

Department of Chemical Engineering,

University of California Santa Barbara

Santa Barbara, California 93106 USA

Carlos J. García-Cervera and Hector D. Ceniceros

Department of Mathematics, University of California Santa Barbara

Santa Barbara, California 93106 USA

(Dated: January 18, 2006)

Abstract

We consider the behavior of the Doi-Marrucci-Greco (DMG) model for nematic liquid crystalline polymers in planar shear flow. We found the DMG model to exhibit dynamics in both qualitative and quantitative agreement with experimental observations reported by Larson and Mead [*Liquid Crystals*, 15 (1993), pp. 151–169] for the Ericksen number and Deborah number cascades. For increasing shear rates within the Ericksen number cascade, the DMG model displays four distinct regimes: stable simple shear, stable roll cells, irregular structure followed by large-strain disclination formation, and irregular structure preceded by disclination formation. In accordance with experimental observations, the model also predicts both ± 1 and $\pm 1/2$ disclinations. Although ± 1 defects form via the *ridge-splitting* mechanism first identified by Feng, Tao, and Leal [*J. Fluid Mech.*, 449 (2001), pp. 179–200], a new mechanism is identified for the formation of $\pm 1/2$ defects. Within the Deborah number cascade, with increasing Deborah number, the DMG model exhibits a stream-wise banded texture, in the absence of disclinations and roll cells, followed by a monodomain wherein the mean orientation lies within the shear plane throughout the domain.

I. INTRODUCTION

The potential for application of liquid crystalline polymers (LCPs)^{1,2,3} as a structural material relies upon the fact that there is a high degree of alignment at both the molecular and mesoscopic levels. The relative *order* within the material is a strong function of its processing history. In fibre spinning flows, the flow is largely extensional and this enhances the natural tendency of the LCP to exist in an aligned state. A result is the well-known Kevlar fibre produced by DuPont. Unfortunately, the processing of LCPs in other configurations is limited by the fact that there is a propensity for the formation and proliferation of orientational defects, known as disclinations, especially in the shear-type flows that are characteristic of most other polymer processing applications. The result in these cases is a material that is isotropic at the mesoscopic level, with alignment confined to small microdomains, and the intrinsic advantage of LCPs as a structural material (which might otherwise offset its increased cost compared to other polymeric materials) is lost. Therefore, to realize the full potential of LCPs, we must understand the processes by which disclinations are formed, and the dependence of these processes on the flow conditions. Because of the small-scale nature of the instabilities that lead to defects in LCPs, the usefulness of macroscopic experimental studies of such instabilities is limited. Reliance is, therefore, placed on theory and numerical investigations for detailed insight into the topological evolution of liquid crystalline systems. Mesoscale numerical investigations, in which a continuum description couples the microscale structure to the macroscopic stress, allow for qualitative prediction of the effects of flow conditions on the formation of disclinations.

Nematic LCPs exhibit both elastic and viscoelastic characteristics when subjected to flow. Both elasticity and viscoelasticity in this class of materials, emanate from the equilibrium tendency for alignment in a uniform direction. Elasticity is associated with the resistance to the formation of

spatial gradients in the mean molecular orientation, and is generally known as *Frank* or *gradient elasticity*⁴. Viscoelasticity derives from flow-induced deviations in the degree of alignment at each point from its equilibrium value. Corresponding to these two manifestations of elastic effects, there are two dimensionless measures of the shear rate for flows of liquid crystalline polymers. The first, known as the Ericksen number² Er , is a ratio of the magnitude of viscous shear stress to the elastic stress. The second is known as the Deborah number⁵ De , and is the product of the shear rate and the natural relaxation time for re-establishment of an equilibrium orientation state. In real systems, the Ericksen number is generally several orders of magnitude larger than the Deborah number at any fixed shear rate.

Although there have been many experimental investigations of the behavior of LCPs in planar shear flow^{6,7,8,9,10,11,12,13}, the most comprehensive, in terms of observations over a wide range of shear rates (and thus also a wide range of Ericksen and Deborah numbers) is the study of Larson and Mead^{10,11} in which a nematic liquid crystalline poly(γ -benzyl-glutamate) (PBG) solution was subjected to shear flows in torsional and planar cells. Larson and Mead¹¹ observed that this LCP exhibited two distinct regimes when subjected to shear flow, which are now believed to be generic to all LCPs. The two regimes are referred to as the Ericksen number and Deborah number cascades. The Ericksen number cascade corresponds to the regime of shear rates where $Er \geq \mathcal{O}(1)$ and $De \ll 1$ and is characterized by instabilities that arise at low shear rates as a consequence of the competition between the viscous stress imposed by the flow and long-range (gradient) elasticity. The result at moderate Ericksen numbers is the formation of roll cells with their axis in the flow direction; followed, as the shear rate is increased by increasingly complex time-dependent flows; and ultimately, to the evolution of disclinations that proliferate with time and lead to a poly-domain structure in which the system is only aligned in small microdomains but is isotropic on larger length scales. During this whole series of flow types, the Deborah number remains small,

though the Ericksen number can achieve quite large values. However, as the shear rate is increased further, the Deborah number reaches $\mathcal{O}(1)$ (and even larger) values, meaning that the time scale characteristic of deformation by the flow (i.e. $\dot{\gamma}^{-1}$) becomes comparable to (or smaller than) the relaxation time scale of the polymer, and viscoelastic effects become important. In this regime, as De is increased, the polydomain structure at first becomes increasingly refined, but eventually, at high enough shear rates, viscoelasticity appears to stabilize the system, the complex polydomain structure disappears and there is again the visual appearance of bands in the flow direction (due to modulations in the mean orientation rather than roll cells), followed at higher shear rates by what is apparently a monodomain structure (no birefringence). The latter series of transitions is the Deborah number cascade.

The numerical investigation presented here, together with the earlier study of Sgalari, Meiburg, and Leal¹⁴, is a first step in the development of computational tools that can be used to simulate the behavior of nematic LCPs in flow. It is focused on a specific molecular model for nematic LCPs^{15,16} with the objective of testing this model and the necessary numerical methods for their ability to reproduce the Ericksen and Deborah number cascades in a simple, two-dimensional shear cell. Before attempting more complex flows, it is important for us to first verify that the molecular theory is capable of predicting the onset and evolution of both types of disclinations (i.e. the *thicks* and *thins* seen experimentally). Previous numerical investigations of the shear flow behavior of nematic LCPs that account for both the local and non-local contributions to the macroscopic stress (i.e., viscoelasticity and gradient elasticity) using either molecular-based models^{17,18,19} or phenomenologically-based tensor models^{20,21,22,23} have been limited to one- or two-dimensional flows between parallel plates wherein the flow is either decoupled simple shear (i.e., the flow is fixed) or coupled flow calculations in which the polymer dynamics are restricted to the shear plane. The calculations reported here consider the coupled-flow problem, in which the

flow and polymer dynamics are coupled via to the macroscopic stress, and are limited only in the sense that they assume “a priori” that there are no spatial gradients in the flow direction.

The majority of previous theoretical and numerical predictions of the onset and growth of roll cells in shearing flows of nematic polymers were limited to the Leslie-Ericksen (LE) theory^{24,25}, which is known to exhibit gradient elasticity but no viscoelasticity. This limits the study to the so-called Ericksen cascade, i.e. to the limiting case $De \rightarrow 0$. In a recent study, Feng, Tao, and Leal²⁵ carried out a numerical investigation of this cascade using the LE theory. Their results demonstrated the onset of the roll-cell formation, followed by de-stabilization of the roll cells and finally the formation of ± 1 disclinations. An initial attempt to generalize these results by including viscoelastic effects via the DMG model was carried out by Sgalari, Leal, and Meiburg¹⁴, following work by Feng, Sgalari, and Leal¹⁶ to derive the constitutive equation corresponding to the Marrucci-Greco extension of the Maier-Saupe Nematic potential¹⁵. As was demonstrated by Feng et al.¹⁶, in the limit $De \rightarrow 0$, the DMG theory reduces to the LE theory. Although the simulations of Sgalari et al. showed promise that the DMG model would capture the expected qualitative behavior for both the Ericksen and Deborah number cascades, numerical issues limited both the range of parameters studied and the accuracy of the simulations.

The present investigation extends the work of Sgalari et al.¹⁴. Improved numerical methods have allowed for more accurate solutions over a much wider range of parameters. However, though the velocity field is 3D in the sense that all three velocity components are nonzero, we have retained the *2D assumption* of no spatial gradients in the flow direction. In the present work, we show that computations carried out at low De do largely reproduce the results found by Feng et al.²⁵ using the LE model. More importantly, we show that the DMG model does produce both ± 1 and $\pm 1/2$ disclinations for large Er and small, but nonzero values of De . Furthermore, as De is increased, the flow is stabilized when viscoelastic effects become strong enough, just as expected

qualitatively from the experimental observations of Larson and Mead¹¹.

II. THEORY AND NUMERICAL METHOD

A. The DMG model

The model used in this study is an extension, due to Marrucci and Greco¹⁵ and Feng et al.¹⁶, of the molecular model first proposed by Doi²⁶, which treats the LCP as a suspension of rigid rod-like molecules having an infinite length-to-width ratio. The forces acting on the rods are hydrodynamic, Brownian, and intermolecular forces. The dynamics of the system of rods is described in terms of an orientational distribution function $\psi(\mathbf{u}; \mathbf{r}, t)$, which gives the probability of finding a rod at position \mathbf{r} with an orientation, represented by the unit vector \mathbf{u} , within the solid angle $d\mathbf{u}$ at time t and is defined such that $\int_{S^2} \psi(\mathbf{u}; \mathbf{r}, t) d\mathbf{u} = 1$, where S^2 is the unit sphere in \mathbb{R}^3 .

If translational diffusion is neglected and the number density of the polymer molecules ν is assumed not to vary in space, the dynamic equation governing the distribution function ψ may be written as²⁷:

$$\frac{\partial \psi}{\partial t} + \mathbf{v} \cdot \nabla \psi = -\mathcal{R} \cdot (\mathbf{u} \times \boldsymbol{\kappa} \cdot \mathbf{u} \psi) + \bar{D}_r \mathcal{R} \cdot \left[\mathcal{R} \psi + \frac{\psi}{k_B T} \mathcal{R} \phi \right], \quad (1)$$

where \mathcal{R} is the rotational operator, $\mathcal{R} = \mathbf{u} \times (\partial/\partial \mathbf{u})$, that corresponds to the gradient operator in rotational diffusion²⁸, $\boldsymbol{\kappa} = (\nabla \mathbf{v})^T$ is the transpose of the velocity gradient, k_B is the Boltzmann constant, T is the absolute temperature, and ϕ is the mean-field nematic potential. Following Doi²⁶, we use a pre-averaged approximation for the rotational diffusivity \bar{D}_r of the form:

$$\bar{D}_r = \frac{D_r}{(1 - S^2)^2}, \quad (2)$$

where D_r is the rotational diffusivity for an isotropic solution having the same polymer concentration. $S = [(3\mathbf{A} : \mathbf{A} - 1)/2]^{1/2}$ is the scalar order parameter, where $\mathbf{A} = \int_{S^2} \psi \mathbf{u} \mathbf{u} d\mathbf{u} = \langle \mathbf{u} \mathbf{u} \rangle$

is the second moment of the distribution function. The colon represents the contraction operator, i.e. $\mathbf{A} : \mathbf{A} = A_{ij}A_{ji}$ with the summation convention, and $\mathbf{u}\mathbf{u}$ is the dyadic tensor product, i.e. $(\mathbf{u}\mathbf{u})_{ij} = u_i u_j$. In effect, Equation (2) accounts for increased rotational diffusivity with increased local order.

The extended Doi theory (which we refer to here as the Doi-Marrucci-Greco theory) incorporates the Marrucci-Greco potential¹⁵ to account for nonlocal elastic contributions analogous to the Frank elasticity contributions of the Leslie-Ericksen theory; the mean-field molecular interaction proposed by Marrucci and Greco couples the Maier-Saupe excluded-volume potential^{29,30} to a non-local potential to account for long-range elastic interactions. The one-constant approximation of the Marrucci-Greco potential, analogous to the $K_{11} = K_{22} = K_{33}$ approximation for the Leslie-Ericksen theory, is given by

$$\phi_{\text{MG}} = -\frac{3}{2}Uk_B T \left(\mathbf{A} + \frac{\ell^2}{24} \nabla^2 \mathbf{A} \right) : \mathbf{u}\mathbf{u}, \quad (3)$$

where ℓ is the persistence length of the distortional elasticity interaction and U is a constant representing the strength of interactions between molecules.

As was proposed by Doi and Edwards²⁷, we represent the polymer stress $\boldsymbol{\tau}$ as the sum of a viscous stress $\boldsymbol{\tau}_v$ and an elastic stress $\boldsymbol{\tau}_e$. The viscous stress remains the same as in the original Doi theory because it is only a result of viscous friction. The more complicated elastic stress contribution, formulated by Feng et al.¹⁶, may be written as

$$\boldsymbol{\tau}_e = 3\nu k_B T \left\{ \mathbf{A} - U (\mathbf{A} \cdot \mathbf{A} - \mathbf{A} : \mathbf{Q}) - \frac{U\ell^2}{24} \left[\mathbf{A} \cdot \nabla^2 \mathbf{A} - \mathbf{Q} : \nabla^2 \mathbf{A} + \frac{\nabla \mathbf{A} : (\nabla \mathbf{A})^T - \nabla \nabla \mathbf{A} : \mathbf{A}}{4} \right] \right\}, \quad (4)$$

where $\mathbf{Q} = \int_{S^2} \psi \mathbf{u}\mathbf{u}\mathbf{u}\mathbf{u} d\mathbf{u} = \langle \mathbf{u}\mathbf{u}\mathbf{u}\mathbf{u} \rangle$ is the fourth moment of the distribution function and the contraction operations are defined as $\nabla \mathbf{A} : (\nabla \mathbf{A})^T = (\partial A_{kl} / \partial x_i) (\partial A_{lk} / \partial x_j)$ and $\nabla \nabla \mathbf{A} : \mathbf{A} =$

$(\partial^2 A_{kl}/\partial x_i \partial x_j) A_{lk}$. The total stress is therefore

$$\boldsymbol{\tau} = \boldsymbol{\tau}_e + \frac{\beta}{(\nu L^3)^2} \left(\frac{\nu k_B T}{2D_r} \right) \boldsymbol{\kappa} : \mathbf{Q}, \quad (5)$$

where $(\nu L^3)^2$ is the crowdedness factor and β is an $O(10^3)$ constant²⁷.

B. Closure approximation

Given that the stress tensor is only a function of the second and fourth moments of ψ (i.e., \mathbf{A} and \mathbf{Q} , respectively), we choose to make some mathematical simplifications in deriving a closed system of equations representing equations (1), (4), and (5) in terms of \mathbf{A} . Following the Prager procedure³¹, we multiply equation (1) by $\mathbf{u}\mathbf{u}$ and integrate over configuration space (i.e., the surface of a unit sphere), to obtain a dynamical equation for the second moment tensor;

$$\begin{aligned} \frac{\partial \mathbf{A}}{\partial t} + \mathbf{v} \cdot \nabla \mathbf{A} &= \boldsymbol{\kappa} \cdot \mathbf{A} + \mathbf{A} \cdot \boldsymbol{\kappa}^T - 2\boldsymbol{\kappa} : \mathbf{Q} \\ &- 6\bar{D}_r \left(\mathbf{A} - \frac{\mathbf{I}}{3} \right) + 6\bar{D}_r (\mathbf{A} \cdot \mathbf{A} - \mathbf{A} : \mathbf{Q}) \\ &+ \frac{\bar{D}_r U \ell^2}{8} (\nabla^2 \mathbf{A} \cdot \mathbf{A} + \mathbf{A} \cdot \nabla^2 \mathbf{A} - 2\nabla^2 \mathbf{A} : \mathbf{Q}), \end{aligned} \quad (6)$$

where \mathbf{I} is the identity matrix. In order to obtain a closed system for \mathbf{A} , we approximate \mathbf{Q} as a function of \mathbf{A} . Such a closure expression yields a closed system of equations [i.e., equations (4), (5), and (6)] that can be coupled to the equations of motion to describe the dynamics of a nematic liquid polymer under an imposed flow.

In approximating \mathbf{Q} , we have chosen to use the so-called Bingham closure approximation³². Numerical investigations by Feng et al.³³ suggest that the Bingham closure model is an appropriate choice in simulating complex flows. Because it is formulated using the simplifying assumption that the probability distribution function can be approximated in the form of a Bingham distribution, the Bingham closure model is only exact in the limit of weak flows where the viscous torque on molecules is not sufficient to skew the orientational distribution, i.e. in the limit of low

De . This limitation results from the fact that the Bingham distribution is inherently restricted to a description of the orientational distribution that exhibits axial symmetry (i.e., uniaxial, biaxial, or triaxial symmetry). The model, therefore, cannot capture the shear-induced *wagging-to-flow-aligning* transition that is observed experimentally at high De ¹¹. Instead, the Bingham closure predicts a monotonic decrease in the wagging amplitude. But, given that tumbling, not wagging, is considered to be the source of disclinations and other defects in dynamic LCP systems, this deficiency in the Bingham closure does not inhibit its application in this context.

C. Governing equations

In making equations (4), (5), and (6) dimensionless, we take the relative velocity V between the shearing plates to be the characteristic velocity, and the plate separation H to be the characteristic length. For the flow considered here, the appropriate characteristic time is H/V . Based on this choice of characteristic scales, the dimensionless constitutive equation and equations of motion may be written as

$$\begin{aligned} \frac{\partial \mathbf{A}}{\partial t} + \mathbf{v} \cdot \nabla \mathbf{A} = & \kappa \cdot \mathbf{A} + \mathbf{A} \cdot \kappa^T - 2\kappa : \mathbf{Q} \\ & - \frac{f}{De} \left(\mathbf{A} - \frac{\mathbf{I}}{3} \right) + \frac{fU}{De} (\mathbf{A} \cdot \mathbf{A} - \mathbf{A} : \mathbf{Q}) \end{aligned} \quad (7)$$

$$\begin{aligned} & + \frac{f}{2cS_{eq}^2} \frac{1}{Er} (\nabla^2 \mathbf{A} \cdot \mathbf{A} + \mathbf{A} \cdot \nabla^2 \mathbf{A} - 2\nabla^2 \mathbf{A} : \mathbf{Q}), \\ Re \left(\frac{\partial \mathbf{v}}{\partial t} + \mathbf{v} \cdot \nabla \mathbf{v} \right) = & \nabla^2 \mathbf{v} - \nabla p + \nabla \cdot \boldsymbol{\tau}, \end{aligned} \quad (8)$$

$$\nabla \cdot \mathbf{v} = 0, \quad (9)$$

where $f = 4/9(1 - \mathbf{A} : \mathbf{A})^{-2}$, $c = \nu k_B T / 2\eta D_r$ is the concentration parameter, and the nondimensional polymeric stress is given by

$$\begin{aligned} \boldsymbol{\tau} = & \frac{c\beta}{(\nu L^3)^2} \boldsymbol{\kappa} : \mathbf{Q} + \frac{c}{De} [\mathbf{A} - U(\mathbf{A} \cdot \mathbf{A} - \mathbf{A} : \mathbf{Q})] \\ & - \frac{1}{S_{eq}^2 Er} \left[\nabla^2 \mathbf{A} \cdot \mathbf{A} - \mathbf{Q} : \nabla^2 \mathbf{A} + \frac{\nabla \mathbf{A} : (\nabla \mathbf{A})^T - \nabla \nabla \mathbf{A} : \mathbf{A}}{4} \right]. \end{aligned} \quad (10)$$

The Reynolds number is defined as $Re = \rho V H / \eta$, with ρ and η being the density of the fluid and the constant solvent viscosity, respectively. Typically, $Re \sim 10^{-3} - 10^{-4}$ for systems similar to that which is considered here. We therefore use the Stokes form of the momentum equation, i.e. equation (8) with $Re = 0$.

The equilibrium value of the scalar order parameter S_{eq} is determined via substitution of the equilibrium (i.e., uniaxial) form for the second moment tensor

$$\mathbf{A}_{eq} = S_{eq} \left(\mathbf{n}\mathbf{n} - \frac{\mathbf{I}}{3} \right) + \frac{\mathbf{I}}{3}, \quad (11)$$

with $\mathbf{n} = (1 \ 0 \ 0)^T$, into the steady, homogeneous form of equation (6).

The pressure and stress have been scaled by $\eta V / H$. Note that dimensional analysis yields two characteristic parameters. The first is the Deborah number De , defined as

$$De = \frac{V/H}{6D_r}, \quad (12)$$

is a ratio of the molecular relaxation time scale to the mean shear rate associated with the flow.

The second is the Ericksen number Er , defined as

$$Er = \left(\frac{24H^2}{cU\ell^2 S_{eq}^2} \right) \cdot De = \frac{\eta V H}{K}, \quad (13)$$

where $K = \frac{1}{8} \nu k_B T U \ell^2 S_{eq}^2$ is the elastic constant¹⁶, is a ratio of viscous stress to elastic stress.

D. Choice of parameter values

With regard to the parameters that were held constant for this study, we used the following values: $\beta = 1000$, $(\nu L^3)^2 = 2 \times 10^6$, $c = 100$, $U = 6$, and $\ell/H = 8.5 \times 10^{-3}$. The value used for the crowdedness parameter, $(\nu L^3)^2$, is typical of lyotropic systems. For a discussion of representative values of c , we refer the reader to the work of Feng and Leal³⁴. In brief, c is proportional to the ratio of the zero-shear-rate viscosity of the LCP solution to the viscosity of the solvent. Although reported values for c range from $\mathcal{O}(10^5)$ to $\mathcal{O}(10^6)$, depending upon the solvent, since the polymeric stress scales with c , which in turn (via the coupling between the polymer and fluid dynamics) contributes to the stiffness of the governing systems of equations, and the fact that we consider Er and De spanning four decades, we use a more conservative value of 100 in this study. In determining the appropriate choice for the nematic strength U , we chose a value so that the DMG model exhibited dynamics that are qualitatively consistent with the PBG solution used by Larson and Mead¹¹. Larson and Mead reported that the PBG solution used in their investigations underwent a *tumbling-to-wagging* transition at $De \approx 2$, followed by a *wagging-to-flow-aligning* transition at $De \approx 5$. As a reference, for the case of the unapproximated Doi theory, which neglects gradient elasticity, $U = 6$ corresponds to these transition De values³³. Since viscoelasticity is the primary driving force behind the dynamics of the model at high shear rates, where $Er \gg 1$ and $De > \mathcal{O}(1)$, we, therefore, have chosen to use $U = 6$ in this investigation. The nondimensional interaction length scale ℓ/H was chosen such that, for the parameter values presented here, $Er/De = 1000$. Therefore, for the results presented here, the only parameters that were varied in the present study were Er and De . For comparison to experiments in which a given polymer is sheared between two parallel plates, with a fixed separation distance, this is equivalent to changes in the shear rate with the ratio Er/De held constant.

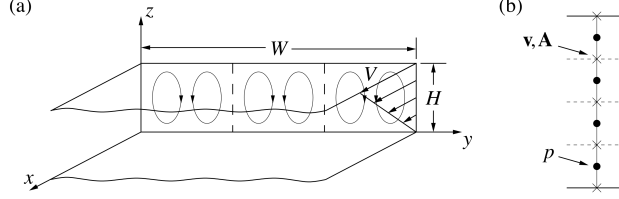


FIG. 1: Schematics of (a) the two-dimensional shear flow domain and (b) the staggered-grid layout along the z -direction. The flow field is bounded along the wall-normal direction by parallel plates separated a distance H and along the span-wise direction by periodic boundaries separated a distance W . V is the relative velocity between the two plates. The velocity and configuration tensor are defined on the regular grid, while the pressure is defined at half-grid points.

E. Discretization

As is depicted in Fig. 1 (a), the computational domain is a rectangular region lying within a plane orthogonal to the primary flow direction (i.e., the y, z -plane) bounded by two parallel plates at $z = 0, 1$ and periodic boundaries at $y = 0, W/H$. The relative velocity between the plates is given as V , and, as previously stated, the characteristic length is taken as H . The domain is discretized in y , the span-wise direction, using a uniform grid spacing h . To cluster grid points near the upper and lower domain boundaries, we utilize the coordinate transformation³⁵

$$z_k = \frac{1}{2} \left\{ 1 + \frac{\tanh [\delta (\xi_k - \frac{1}{2})]}{\tanh (\delta/2)} \right\}, \quad (14)$$

where $\xi_k = \frac{k-1}{N_z-1}$, $k = 1, \dots, N_z$, to generate a non-uniform grid in z , the wall-normal direction. A value $\delta = 2.0$ was used for the results presented in this work. A staggered grid is used, with respect to the z direction [see Fig. 1 (b)], such that the components of \mathbf{v} and \mathbf{A} are defined on the regular mesh, with N_z nodes, and the $N_z - 1$ pressure nodes are staggered at half-grid points. The continuity constraint is enforced at the p -nodes, while the equations of motion and evolution equation for the polymer configuration are solved at the (\mathbf{v}, \mathbf{A}) -nodes.

As the texture length scale decreases with increasing values of the Ericksen number Er , the results presented in Section III were obtained using grid spacings ranging from $h = 1/32$ to

$h = 1/1024$, where $h = \Delta_y = \Delta_\xi$. The mesh was refined until there was no discernable difference in either the transient structure or the time scales associated with the onset of the initial roll cell instability and the ensuing director dynamics for a given initial configuration. An adequate domain width was chosen in a similar manner, with the additional constraint that the aspect ratio of the steady-state or transient roll cells not vary beyond a given value of W/H .

To reduce the size of the numerical problem, we assume that there are no gradients in the stream-wise direction x . The flow is still three-dimensional in the sense that all three components of \mathbf{v} are non-zero and we consider the general form for \mathbf{A} at each point. The implications of the assumption of no gradients in x will be discussed in Section IV, following the presentation of our numerical results. Given the periodic boundary conditions imposed at $y = 0, W/H$, we use spectral collocation for the flow and configuration components in the span-wise direction. Derivatives, with respect to the y -direction, are therefore evaluated efficiently via the fast Fourier transform. Wall-normal derivatives are evaluated using a second-order finite difference formulation. The steady-Stokes form of equation (8) is solved using the Uzawa Bi-Conjugate Gradient Stabilized³⁶ method, the details of which are presented in a previous paper³⁷. We integrate the evolution equation for the polymer configuration (7) using the second-order Runge-Kutta TVD scheme proposed by Shu and Osher³⁸.

F. Boundary and initial conditions

No-slip conditions are imposed on the velocity components at $z = 0, 1$, i.e., $\mathbf{v} = (v_x \ v_y \ v_z)^T = (z \ 0 \ 0)^T$. With regard to boundary conditions for the configuration tensor \mathbf{A} , the polymer configuration is *anchored* along the upper and lower boundaries of the domain such that the \mathbf{A} remains fixed in its uniaxial form [i.e., equation (11), with $\mathbf{n} = (0 \ 1 \ 0)^T$]. Initial conditions for the velocity components are those of linear shear flow, where $\mathbf{v}(\mathbf{x}, t = 0) = (z \ 0 \ 0)^T$. A random-phase per-

turbation, with an $\mathcal{O}(10^{-6})$ amplitude, is introduced into polymer configuration, which is initially defined such that the mean orientation is along the y -direction. These boundary conditions are consistent with both the LE theory analyses^{24,25} and experiments of Larson and Mead^{10,11}. Given an initial orientation along the vorticity axis, these studies found the earliest-observed instability to be that of roll cells and, with regard to the experimental observations, accompanying birefringent stripes oriented along the flow direction. For initial mean orientations along either the velocity gradient or flow directions, although the roll-cell instability is observed later in time, Larson and Mead reported that the earliest instability observed was the formation of a banded pattern oriented along the vorticity axis and periodic along the flow direction. Since the variation in structure is along the flow direction, such an instability cannot be captured in this investigation.

III. NUMERICAL RESULTS

We have found that the DMG model exhibits dynamics that are in qualitative agreement with both experimental^{10,11} and applicable theoretical and numerical investigations^{24,25,39}. As previously mentioned, the only parameters varied in our calculations are De and Er . Given that the ratio Er/De is held constant, reference will primarily be made to changes in the Ericksen number for the results presented here. In the context of the LE theory, the average orientation, referred to as the director, is described using the unit pseudo-vector \mathbf{n} , i.e. \mathbf{n} and $-\mathbf{n}$ are energetically equivalent. For the DMG theory, the average orientation can be associated with the eigenvector representative of the largest eigenvalue of \mathbf{A} . To distinguish this difference between the two different models, we describe the director using the unit pseudo-vector \mathbf{d} .

A. Low to moderate shear rates, $Er \lesssim 6000$ ($De \lesssim 6$)

For the case of low to moderate shear rates, the polymer and coupled fluid dynamics are primarily a function of the contribution of gradient elasticity to the macroscopic stress. Arguably, the effects of viscoelasticity are non-negligible as De approaches and exceeds unity, but our results indicate that the system dynamics and resulting structure are dominated by the so-called Frank stress. For finite Er less than approximately 6000 ($De \lesssim 6$), the responses of the perturbed system, in order of increasing Er , were:

1. Stable simple shear,
2. Stable roll cells,
3. Irregular structure followed by large-strain disclination formation, and
4. Irregular structure preceded by disclination formation.

Due to computational limitations, the range of Er listed for each regime have an associated error of approximately 10 percent.

1. Stable simple shear, $Er \lesssim 40$

For Ericksen values less than approximately 40, the system exhibits stable simple shear with the average polymer orientation along the spanwise direction, generally referred as to the *log-rolling* configuration, throughout the flow domain. Although there is an initial transient regime, during which the director precesses about the vorticity axis, the amplitude of these rotations slowly decreases over time as $\mathbf{d} \rightarrow (0 \ 1 \ 0)^T$.

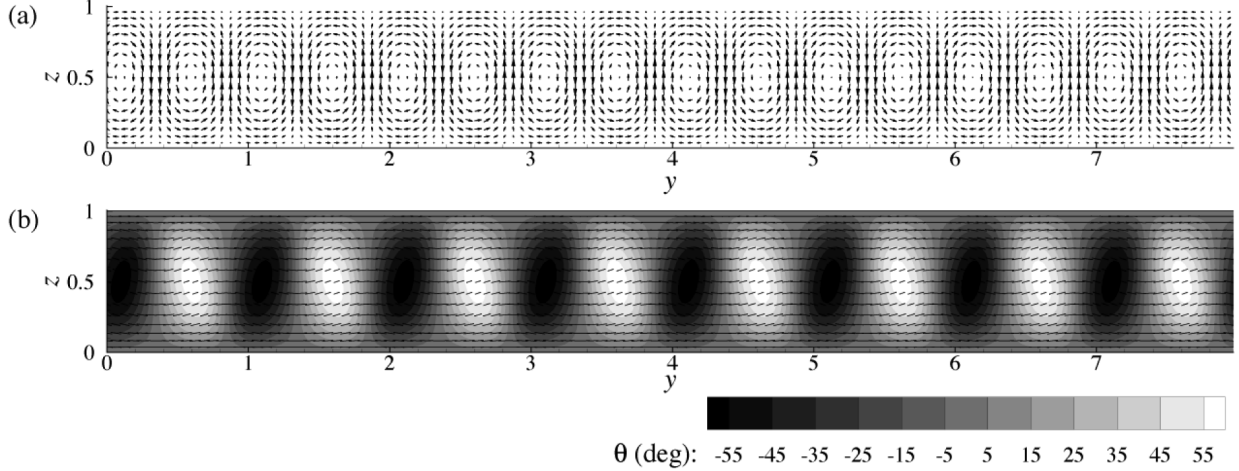


FIG. 2: Steady-state (a) secondary flow vector field (v_y, v_z) and (b) director vector field $\mathbf{d}(\mathbf{x})$ and tip angle θ scalar contour for $Er = 50$ ($De = 0.05$). Note: a color animation showing the evolution of the system to this final state can be accessed by selecting the figure image.

2. Stable roll cells, $40 \lesssim Er \lesssim 250$

As the shear rate is increased, the perturbed orientation field becomes unstable, via a mechanism associated with anisotropy of the viscous stress for a sheared nematic⁴⁰, to the formation of roll cells. The flow structure is that of paired, counter-rotating vortices oriented along the flow direction. The director exhibits modulation in its orientation, with respect to the computational plane (i.e., the y - z plane), along the span-wise direction. An example of the stable flow and orientation configurations, for $Er = 50$, is presented in Fig. 2. The angle between the director and the y - z plane, which we refer to here as the tip angle, is given as θ .

For $Er = 50$, the (height-to-wide) aspect ratio of the steady-state roll-cell structure is $AR = 2.0$, and the maximum value of the steady-state secondary flow, relative to the primary flow, is 0.012. The largest deviation of the director from the computational plane $|\theta|_{\max}$ of approximately 60 degrees occurs at the center of the roll cells, where the magnitude of the vorticity associated with the secondary flow reaches a maximum. The evolution of the director orientation \mathbf{d} , as a function of strain units τ , within the center of a roll cell [at $(y, z) = (4.62, 0.5)$ in Fig. 2] is

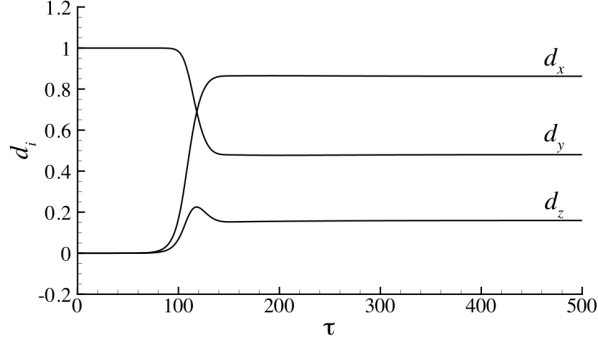


FIG. 3: Evolution of director components at $(y, z) = (4.62, 0.5)$, for $Er = 50$ ($De = 0.05$).

presented in Fig. 3. As was observed in the LE calculations of Feng et al.²⁵, a log-log plot of the data presented in Fig. 2 shows that the growth of the instability is exponential at the outset, but becomes linear at a given strain, prior to reaching steady state. For $Er = 50$, this transition in the growth rate occurs at $\tau \approx 80$ strain units, and steady state is reached at $\tau \approx 160$ strain units.

Qualitatively, there was no difference in dynamics for the cases we studied within this regime. As the Ericksen number was increased, there was a corresponding increase in the aspect ratio of the resulting roll cells, increase in the tip of the director away from the computational plane within roll-cell vortices, and increase in the rate at which roll cells form. For the range of Ericksen values resulting in stable roll-cell configurations, we observed $1.75 \leq AR \leq 3.50$ and $50 \leq \theta_{\max} \leq 75$ degrees. Quantitatively, the most relevant data, for direct comparisons to experiment, is the scaling of the roll-cell aspect ratio as a function of Er , the details of which will be discussed later in Section IV.

3. Irregular flow and orientation structure with large-strain disclination formation, $250 \lesssim Er \lesssim 1500$

For Er greater than approximately 250, the regularity of the structure observed for lower Er , where a single mode (i.e., roll cells with a single aspect ratio) persists for an indefinite period of time, yields to the intrinsic nonlinearity of the model and the decrease in the elastic contribution to

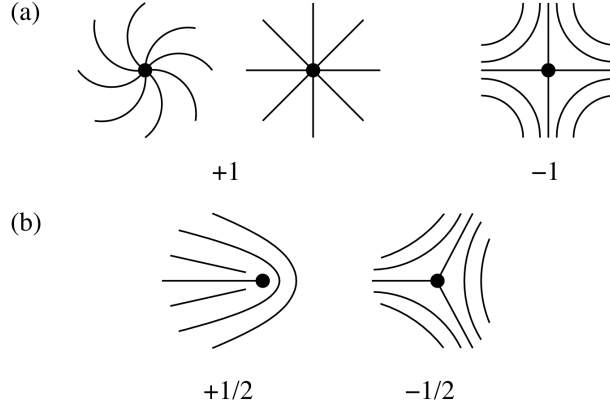


FIG. 4: Schematics of (a) 1-strength and (b) $1/2$ -strength disclinations observed in calculations. The dot represents the defect core, and the lines are the director vector field lines (i.e., lines drawn tangent to the vector field) projected onto the computational domain. The strength and sign correspond to the relative rotation of the director around a path encircling the disclination.

the stress relative to the viscous stress. As the director tips further towards the flow direction, the tendency for the model to exhibit tumbling can no longer be completely inhibited by gradient elasticity. Local fluctuations in the director field lead to a breakdown of the regular roll-cell structure, which then propagates throughout the domain. Given sufficiently high Er values, the resulting irregular flow structure is accompanied by the formation of $1/2$ - and 1-strength orientational defects, depictions of which are presented in Fig. 4. We note that, since they were also obtained using the LE model²⁵, it is expected that we observe ± 1 disclinations, but disclinations of strength $1/2$, however, have not previously been predicted in flow simulations.

As is the case for lower Er , the initial structure is that of roll cells. The distinct difference between this initial *transient* structure and the *steady-state* structure observed at lower Er is that there is not a single roll-cell aspect ratio observed, but a narrow distribution of aspect ratios. As a typical example of the initial roll-cell structure seen within this regime, we present the flow and orientation configurations for $Er = 500$ at $\tau = 35$ strain units in Fig. 5; the dark vertical strips in Fig. 5 (b) correspond to the point where $|\theta| \rightarrow 0$ between adjacent roll cells. The maximum secondary flow velocity, relative to the imposed boundary velocity, is 0.014, and the largest de-

viation of the director from the computational plane $|\theta|_{\max}$ is 78.7 degrees. Although most roll cells within the domain have an approximate aspect ratio of approximately 5, it is evident that $3.13 \leq AR \leq 5.88$.

As previously stated, breakdown of the regular roll-cell structure is a consequence of the inability of gradient elasticity to inhibit temporal modulations, in the form of either wagging or tumbling, within the director field. These modulations are followed by *roll-cell splitting*, where smaller “daughter cells” form as adjacent roll cells split along the z -direction. To clarify the dynamics leading to the onset and propagation of the splitting instability, we present in Fig. 6 an example of the evolutions of the secondary flow and director fields during this process taken from our $Er = 500$ results, where the solution first exhibits roll-cell splitting at $\tau = 40$ strain units. Before the onset of the splitting process, the cells having the smallest aspect ratio (between $1.56 < y < 2.16$) exhibit a slight asymmetry, most notably in the director field, as indicated by the variation in the $|\theta|$ contour in right plot of Fig. 6(a). Given that the induced twist in the orientation field associated with tipping of the director at the roll cell core is, energetically, less favorable for the skinnier cells with larger aspect ratios, it is not surprising that the small-aspect-ratio cells are more susceptible to the instability.

In the cores of the previously mentioned roll cells, the director tips away from the stream-wise direction and toward the y - z plane [note the increase in the length of the director field vectors and dark bands forming in the $|\theta|$ contour along $y = 1.7$ and 2.0 in the plot to the right in Fig. 6(b)]. From the secondary flow field presented in the left plot in Fig. 6(b), we see that as the transition in the orientation field occurs, the roll cells become unstable to splitting. The instability and corresponding perturbation in the orientation field, then, propagates to the left and right [see Fig. 6(c)] as once-stable roll cells and daughter cells formed earlier in the process split to produce vortices of various sizes and strengths. We can estimate the propagation speed of the instability by comparing

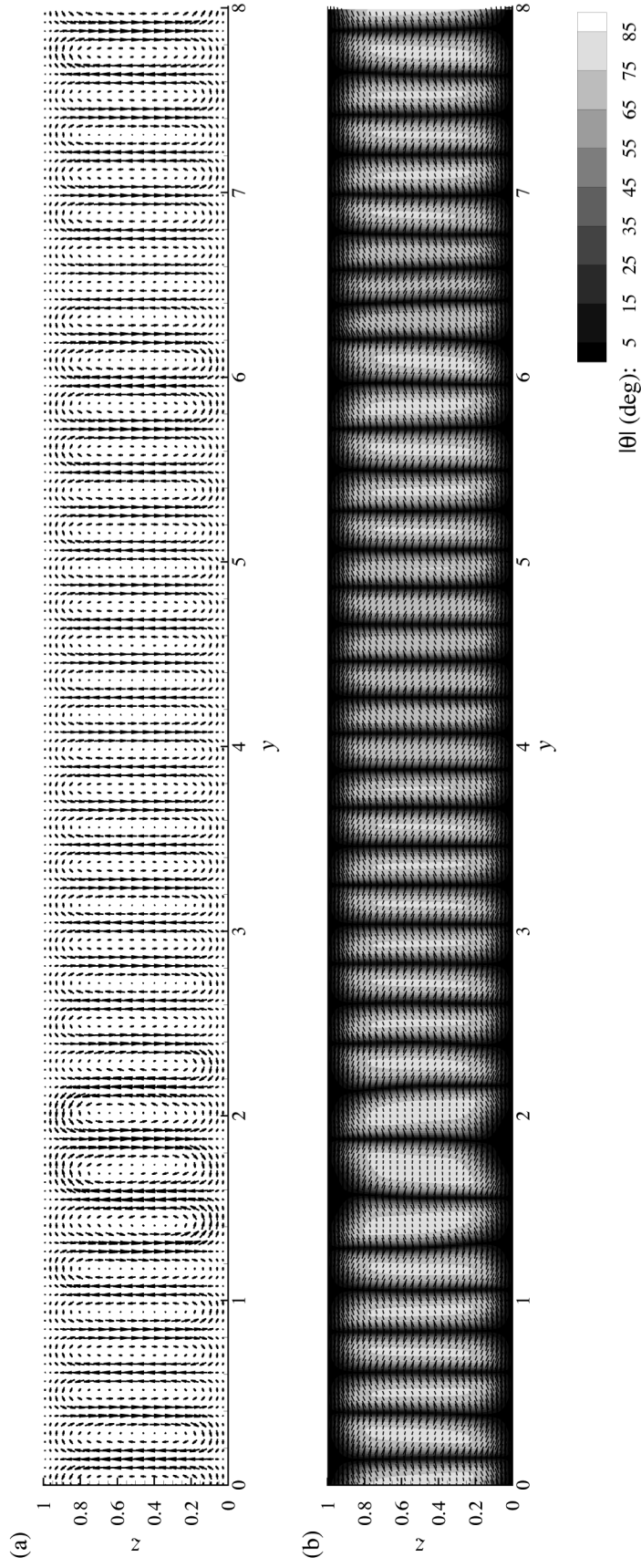


FIG. 5: (a) Secondary flow vector field (v_y, v_z) and (b) director vector field $d(x)$ and tip angle magnitude $|\theta|$ scalar contour for $Er = 500$ ($De = 0.5$) at $\tau = 35$ strain units.

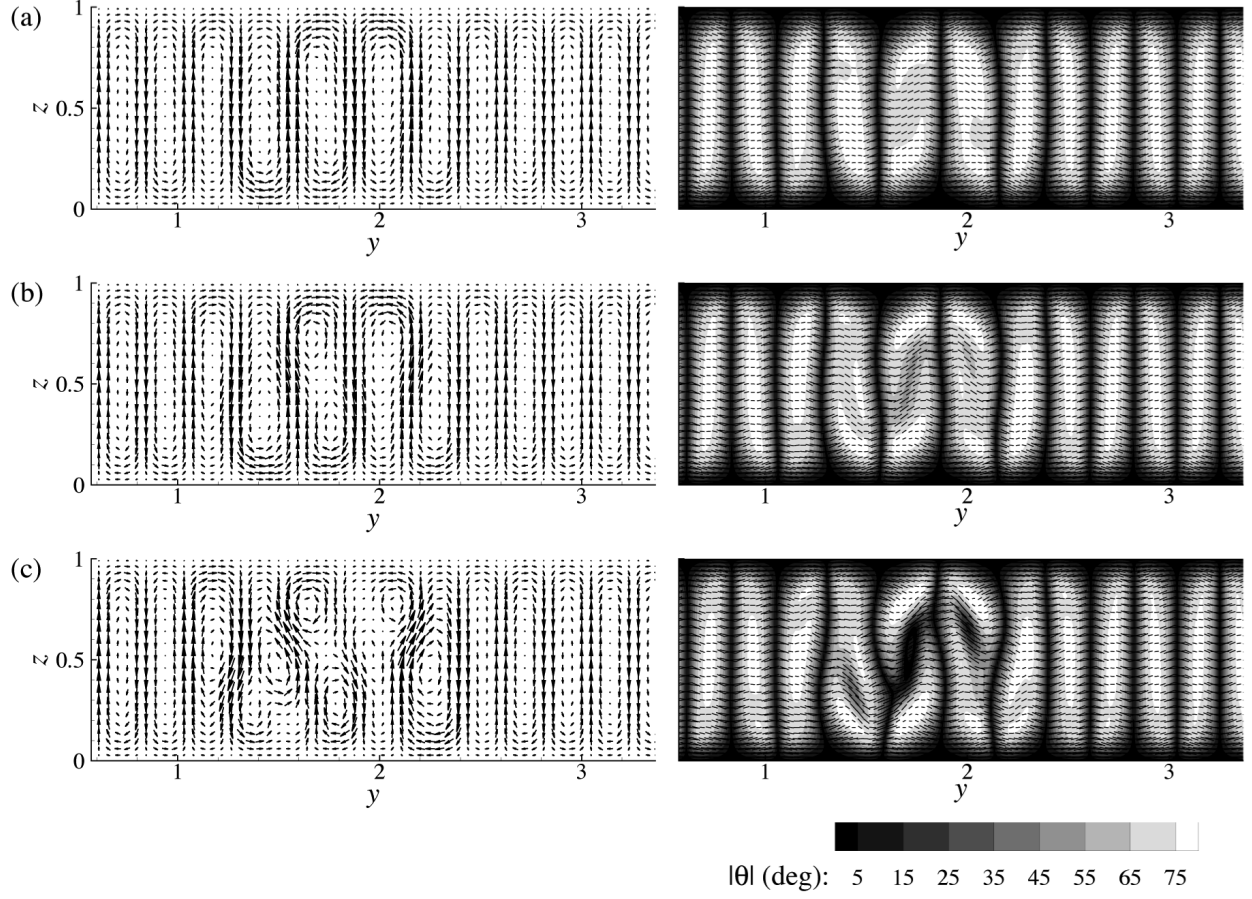


FIG. 6: Roll-cell splitting and propagation for $Er = 500$ ($De = 0.5$). (left) Secondary flow vector field (v_y, v_z) and (right) director vector field $\mathbf{d}(\mathbf{x})$ and tip angle magnitude $|\theta|$ scalar contour at (a) $\tau = 40$, (b) $\tau = 45$, and (c) $\tau = 50$ strain units. Note: a color animation showing the splitting process within the region shown here can be accessed by selecting the figure image.

the director dynamics in the cores of neighboring roll cells along the y -direction. In Fig. 7, we show the director components, as a function of strain units τ , for points corresponding to the center of the roll cell from which the instability originates [Fig. 7(a)] and the center of the third and fifth roll cells [Fig.s 7(b) and 7(c), respectively] to the left of the origin cell. As is evident from comparison of the delay of the initial perturbation of the x -component of the director away from $d_x \approx -1$ in Fig.s 7 (a) through (c), and accounting for the fact that the instability propagates to the left and right, the approximate propagation speed of the instability is $2/50 \tau^{-1}$. In accordance with this approximation, we observed the last cells undergo splitting at $\tau \approx 250$.

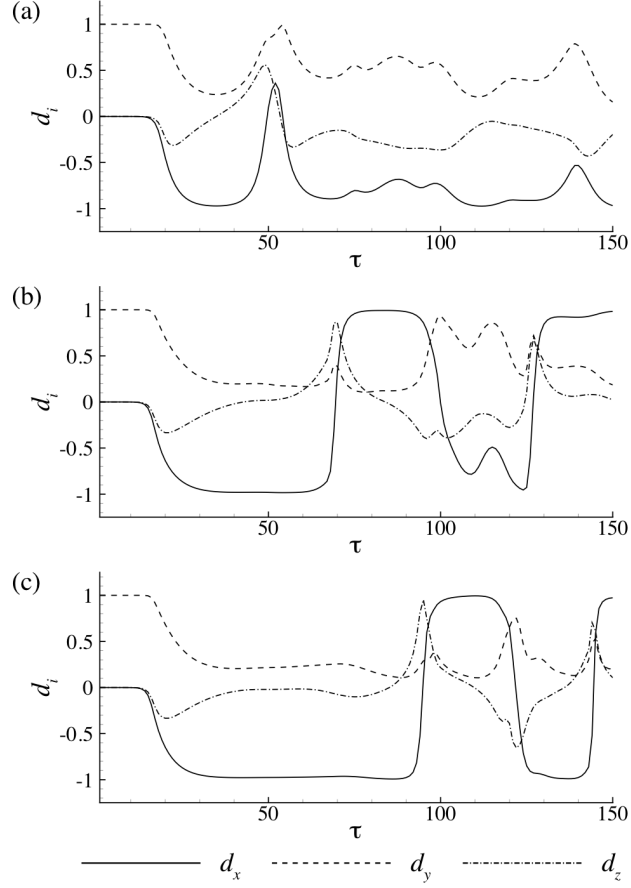


FIG. 7: Evolution of the director at (a) $(y, z) = (1.72, 0.5)$, (b) $(y, z) = (1.16, 0.5)$, and (c) $(y, z) = (0.72, 0.5)$ for $Er = 500$ ($De = 0.5$).

As the instability initiated by roll-cell splitting propagates throughout the computational domain, the irregularity of the flow and orientation structure gives rise to the formation of disclinations. For $Er \lesssim 700$, we observed only the formation of ± 1 disclination pairs, which are formed by the same “ridge-splitting” mechanism first identified in simulations using the Leslie-Ericksen model by Feng et al.²⁵. During this process, localized ridges form within the director field, along which the director is oriented primarily in the flow direction. Given the proper conditions, with regard to the flow and director fields, the ridge splits to form a ± 1 pair of disclinations in what is referred to as the *escaped configuration*, wherein these disclinations have “escaped” a true orientational singularity by rotating at their core into the flow direction without any change in the degree of alignment. As an example of the flow and microstructure just prior to the formation

of a ± 1 disclination pair, we show a snapshot of the secondary flow and director fields for our $Er = 500$ calculation at $\tau = 143$ strain units (the time at which the first defects were observed in this simulation) in Fig. 8. Ellipses in Fig. 8(b) indicate regions containing the aforementioned ridge configurations, as indicated by the shrinking of the director field vector to a point in the ellipse centers and associated transition in the overlaid $|\theta|$ contour from white along the ridge, where $|\theta| \approx 90$ degrees, to darkening shades of grey, indicating a decrease in $|\theta|$, away from the ridge. As eluded to above, the ridge structure does not always lead to the development of disclinations; the highlighted ridge at $y \approx 2.9$ in Fig. 8(b) leads to the formation of a ± 1 pair of defects, the details of which will be discussed below, while the ridge at $y \approx 0.3$ is gone within a few strain units as the local orientation assumes that of the surrounding field.

To aid in discussing the details of ± 1 defect pair formation via the ridge-splitting mechanism, we present the evolution of the flow and director fields during the formation and subsequent annihilation of the first-observed disclinations for the $Er = 500$ results in Fig. 9. We should note that the director field vectors in Fig. 9 have been plotted with a fixed length, rather than their projected length in the y - z plane as in previous figures, so as to emphasize the defect structure. As previously mentioned, the formation of ± 1 disclinations is initiated by the appearance of a ridge structure [highlighted in the director field plot in Fig. 9 (a) by an ellipse] at $\tau = 143$ strain units. We see from comparison of the director field in the right plot of Fig. 9 (b) to the disclination depictions presented in Fig. 4 (b) that, at $\tau = 145$ strain units, the ridge splits to form a ± 1 pair of disclinations. Upon formation, the disclinations move through the domain [Fig. 9 (c)] via hydrodynamic forces as a consequence of flow modification induced by the dynamics of the orientation field and interactive forces resulting from gradient elasticity. After a given amount of time, which ranged from 10 to 20 strain units for the results presented here, the ± 1 disclination pair succumbs to a manifestation of gradient elasticity in the form of an attractive force between

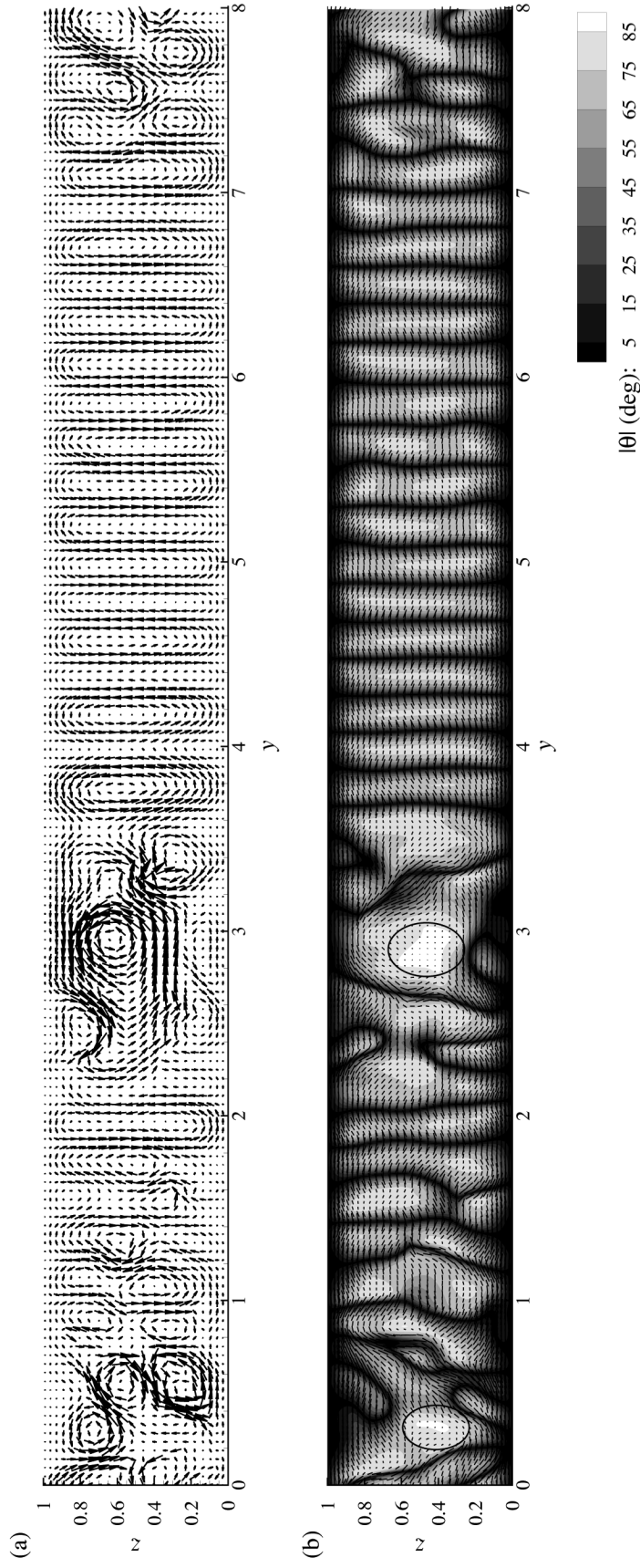


FIG. 8: (a) Secondary flow vector field (v_y, v_z) and (b) director vector field $\mathbf{d}(\mathbf{x})$ and tip angle magnitude $|\theta|$ scalar contour for $Er = 500$ ($De = 0.5$) at $\tau = 143$ strain units, just prior to the formation of the first ± 1 defect pair.

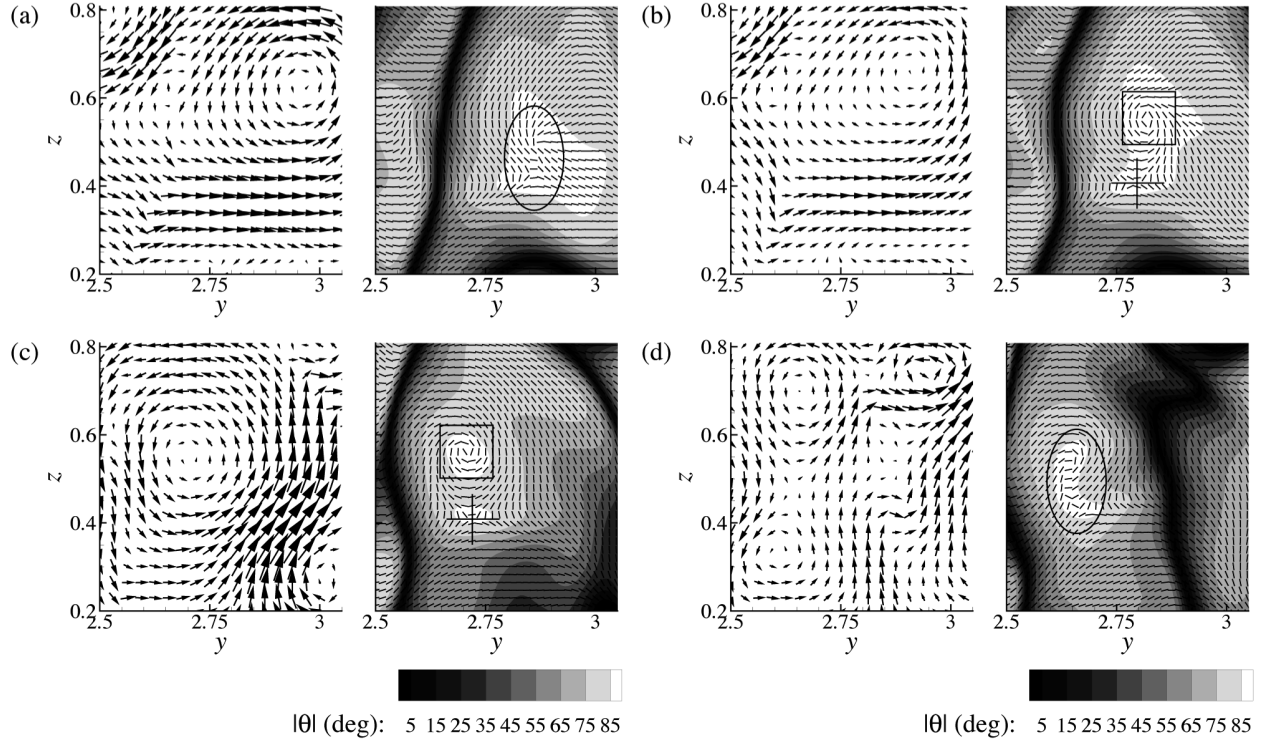


FIG. 9: Initial disclination formation for $Er = 500$ ($De = 0.5$). (left) Secondary flow vector field (v_y, v_z) and (right) director vector field $\mathbf{d}(\mathbf{x})$ and tip angle magnitude $|\theta|$ scalar contour at (a) $\tau = 143$, (b) $\tau = 145$, (c) $\tau = 150$, and (d) $\tau = 154$ strain units. The ellipses highlight the “ridge” structures from which the ± 1 defect pair originates (a) and, at a later time, annihilates via recombination (d). Crosses and squares indicate -1 and $+1$ disclinations, respectively. Note: a color animation showing the dynamics of flow and director fields depicted in this sequence of images can be accessed by selecting the figure image.

oppositely-signed disclinations and annihilation via recombination occurs at $\tau = 154$ strain units [Fig. 9 (d)].

For the example presented here, it appears that the disclination structure is a result of the relatively high-strength roll cell encompassing the region in which the disclination pair resides. As is the case for the regular roll-cell structure, the largest degree of tipping occurs at the cell core, where the magnitude of the vorticity associated with the secondary flow reaches a maximum, possibly aiding in the formation of the ridge structure. There is also a noticeable synchronization between the flow and configuration fields as the disclinations and encompassing roll cell propagate along the span-wise direction within the domain, and the splitting of the large roll cell occurs at approx-

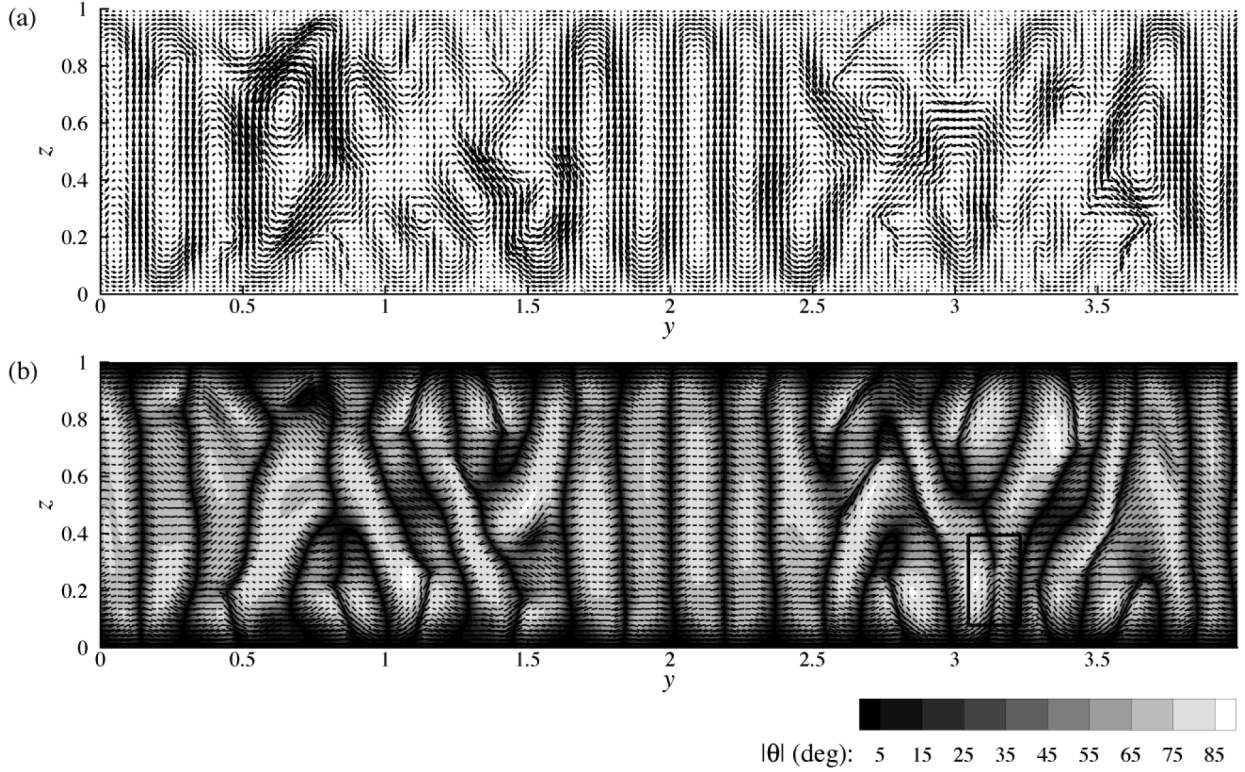


FIG. 10: (a) Secondary flow vector field (v_y, v_z) and (b) director vector field $\mathbf{d}(\mathbf{x})$ and tip angle magnitude $|\theta|$ scalar contour for $Er = 1000$ ($De = 1$) at $\tau = 60$ strain units. Note: a color animation showing the evolution of the flow and microstructure representative of the data presented here can be accessed by selecting the figure image.

imate the same strain at which the disclinations recombine. Although this coupling between the flow and disclination dynamics, in which ± 1 disclination pairs originate in the core of relatively high-strength roll cells, is somewhat generic to this regime, we also observe defect formation via ridge-splitting in regions bridging several vortices and regions between adjacent vortices.

For $Er \gtrsim 700$, we observed the formation of both ± 1 and $\pm 1/2$ disclination pairs. As was the case for lower Er , where we observed only ± 1 disclinations, the initial structure is that of roll cells followed by the breakdown of the regular roll-cell structure via the splitting instability, albeit the required strain for the onset of the instability decreases with increasing Er . However, in this case, as the roll-cell splitting instability propagates throughout the domain, in addition to ± 1 defect pairs generated via the ridge-splitting mechanism, we observe $+1/2$ and $-1/2$ disclinations. As

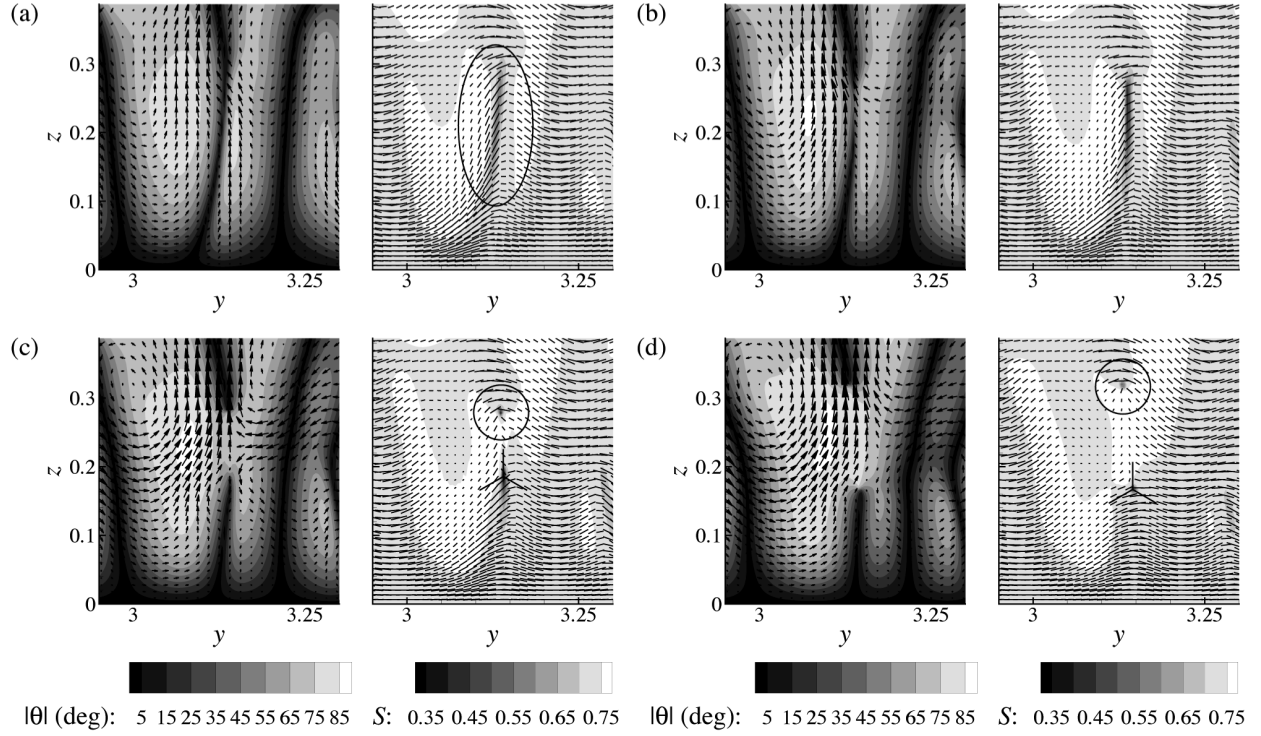


FIG. 11: Disclination formation for $Er = 1000$ ($De = 1$). (left) Secondary flow vector field (v_y, v_z) and tip angle magnitude $|\theta|$ scalar contour and (right) director vector field $\mathbf{d}(\mathbf{x})$ and order parameter S scalar contour at (a) $\tau = 58$, (b) $\tau = 60$, (c) $\tau = 61$, and (d) $\tau = 63$ strain units. The three-armed symbols and circles in (c) and (d) indicate the $+1/2$ and $-1/2$ disclinations, respectively. Note: a color animation of the system dynamics depicted in the series of images presented here can be accessed by selecting the figure image.

an example of the flow and microstructure just during the formation of a pair of $\pm 1/2$ defects, we show the secondary flow and director fields for $Er = 1000$ at $\tau = 60$ strain units in Fig. 10, the strain at which we first observe $1/2$ -strength defects during this simulation. The respective maxima in the secondary velocity and tip angle magnitude are $|\mathbf{v}|_{\text{sec}} = 0.015$ and $|\theta| = 90$ degrees. The region in which we observed the $\pm 1/2$ pair of disclinations is indicated by a rectangle in the lower right corner of Fig. 10 (b).

In discussing the details of the mechanism by which $\pm 1/2$ disclination pairs form, we refer the reader to Fig. 11, in which we show an example of the evolution of the secondary flow and director and order parameter fields during disclination formation from our $Er = 1000$ simulation. At $\tau = 58$ strain units [Fig. 11 (a)], a localized twist develops in the director field, originating

at approximately $(y, z) = (3.14, 0.22)$ (the region about which is indicated by the ellipse), which is accompanied by a reduction in the local order parameter S from the equilibrium value of 0.74 to 0.54. Just prior to the formation of the defect pair, at $\tau = 58$ strain units, the continued strain imposed by the increasing curvature in the director field $\partial^2\theta/\partial z^2$ along $y = 3.14$, as indicated by the narrowing of the dark band in the $|\theta|$ contour in the left plot in Fig. 11 (b), results in a further reduction in the local order parameter S to 0.43. As the amount of stored elastic energy $K\partial^2\theta/\partial z^2$ increases, the localized region becomes susceptible to an instability that lowers the distortional energy at the expense of the energy required for the creation of a defect; specifically, for this case, a $\pm 1/2$ disclination pair. Just following the formation of the defect pair, S reaches local minimum values of 0.34 and 0.25, respectively, at the cores of the $+1/2$ and $-1/2$ disclinations, which can be identified by comparison of the highlighted regions in the director field shown in Fig. 11 (c) to the depictions of the $1/2$ -disclination structures in Fig. 4 (b). Also, there is an abrupt change in the director orientation along $y = 3.1$ at the core of each disclination where the director goes from being oriented along the y -direction above and below the disclination pair to a nearly flow-aligning orientation between them. There is also a noticeable perturbation in the secondary flow field in the vicinity of the $+1/2$ disclination and increase in $\partial v_z/\partial z$ between the two defects as the $+1/2$ disclination moves upwards towards the center of the domain while the $-1/2$ disclination remains stationary. These transitions in the director orientation and changes in the flow brought about by the strong coupling between the flow and microstructure become more pronounced upon formation of the final defect structure [Fig. 11 (d)].

4. Disclination formation prior to flow structure degradation, $1500 \lesssim Er \lesssim 6000$

For $Er \gtrsim 1500$, we observed the formation of ± 1 and $\pm 1/2$ disclinations prior to the breakdown of the initial roll-cell structure. Although the formation of defects is still proceeded by

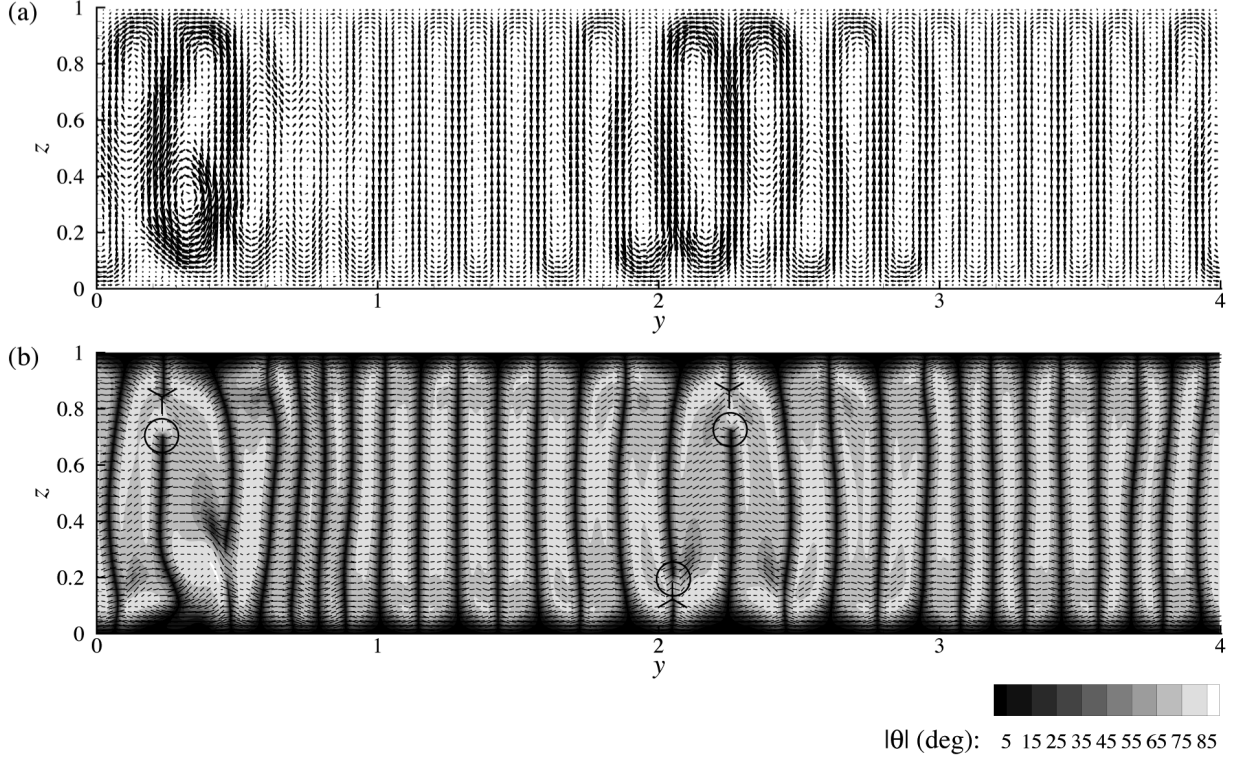


FIG. 12: (a) Secondary flow vector field (v_y, v_z) and (b) director vector field $\mathbf{d}(\mathbf{x})$ and tip angle magnitude $|\theta|$ at $\tau = 39$ strain units for $Er = 2000$. The three-armed symbols and circles indicate the $+1/2$ and $-1/2$ disclinations, respectively. Note: a color animation showing the evolution of the flow and microstructure can be accessed by selecting the figure image.

roll-cell splitting for larger Er within this regime (i.e., for the larger values between 1500 and 6000), the splitting process differs from that observed at lower Er in that, early in the process, the daughter cells remain within the regions originally encompassed by the rolls cells from which they form as the “parent” cells split along the z -direction. Our results indicate that the breakdown of the regular structure, either of roll cells spanning the entire gap height, as is the case for lower Er within this regime, or paired daughter cells in the previously mentioned configuration that are observed for higher Er , is predominantly a consequence of disclination dynamics and the coupling between these dynamics and the flow.

At lower Er within this regime, the defect structure observed at the earliest time (i.e., the least amount of strain) is that of $\pm 1/2$ disclinations that form near the upper and lower domain

boundaries in the convergent region between adjacent roll cells. As will be discussed later in Section IV, this is in qualitative agreement with the findings of Larson and Mead¹¹; they reported that disclinations usually originated and resided between adjacent roll cells within the Ericksen number cascade. A typical example of solutions exhibiting such structure is presented in Fig. 12, wherein we show a snapshot of the velocity and director fields for $Er = 2000$ at $\tau = 39$ strain units. Referring to Fig. 12 (a), one can see that, although some vortices have undergone splitting, the overall roll-cell structure remains relatively intact. In considering the magnitude of the tip angle $|\theta|$, the director orientation is primarily along the flow direction within the roll cells, where $|\theta| \approx 80$ degrees, but is subject to large gradients along the span-wise direction between adjacent cells, where $|\theta| \rightarrow 0$. In convergent regions near the upper and lower boundaries of the domain, there is an increase in curvature of the director field with increased strain as was observed at lower Er . As before, these localized regions become susceptible to an instability that lowers the distortional energy at the expense of the energy required for the creation of a $\pm 1/2$ pair of disclinations. In this case, however, the $-1/2$ disclination remains stationary near the wall as the $+1/2$ moves towards the center of the domain between the adjacent roll cells. At large strain, we also observe ± 1 defect pairs which form via the ridge-splitting mechanism and exhibit dynamics that do not differ, qualitatively, from those seen in solutions for lower Er .

An example of the dynamics of the flow and configuration fields during the early-stage disclination formation for $Er = 2000$ is shown in Fig. 13. At $\tau = 36$ strain units [Fig. 13(a)], the twist in the director field, which originates at approximately $(y, z) = (0.23, 0.82)$, is accompanied by a reduction in the local order parameter S from the equilibrium value of 0.74 to 0.47 to form a low-order core from which the $\pm 1/2$ defect pair emanates (a point we will return to when presenting our results for higher Er within this regime). In Fig. 13(b), just following the formation of the defects, S reaches local minimum values of 0.45 and 0.36, respectively, at the cores of the

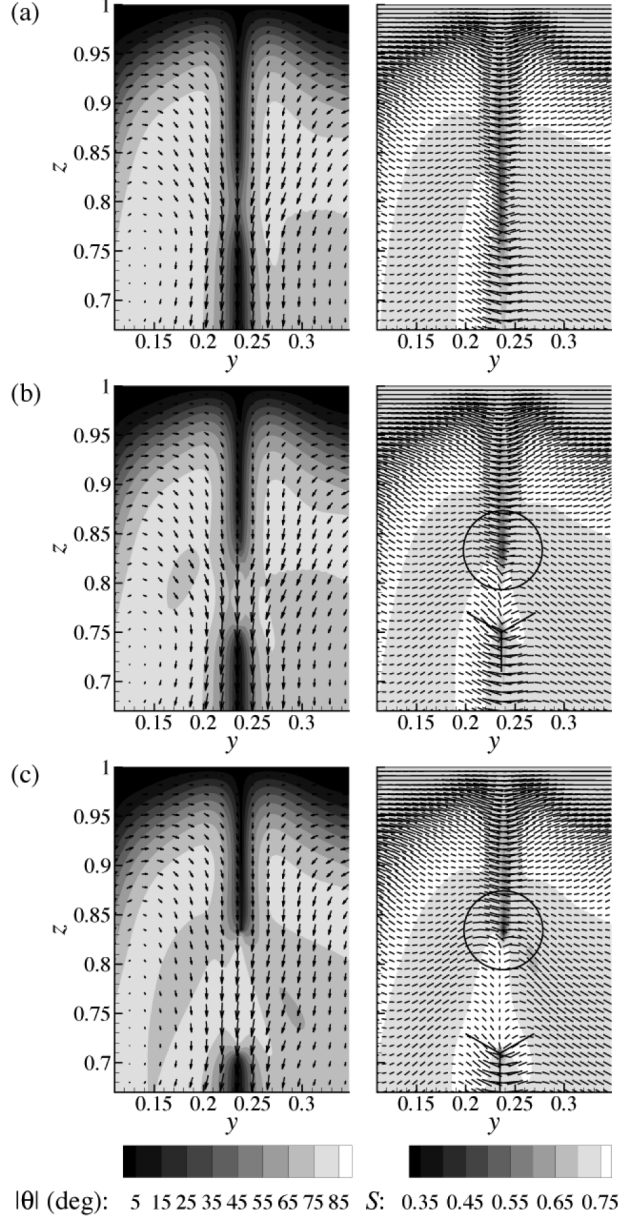


FIG. 13: Early-stage disclination formation for $Er = 2000$ ($De = 2$). (left) Secondary flow vector field (v_y, v_z) and tip angle magnitude $|\theta|$ scalar contour and (right) director vector field $\mathbf{d}(\mathbf{x})$ and order parameter S scalar contour at (a) $\tau = 36$, (b) $\tau = 37$, and (c) $\tau = 39$ strain units. The three-armed symbols and circles indicate the $+1/2$ and $-1/2$ disclinations, respectively. Note: a color animation of the process depicted in this sequence of images can be accessed by selecting the figure image.

$+1/2$ and $-1/2$ disclinations. As was observed for lower Er , although more pronounced here, there is an abrupt change in the director orientation along the centerline between the disclination pair where the director goes from being oriented along the y -direction above and below the disclination pair to a nearly flow-aligning orientation between them. Also, there is, again, a noticeable

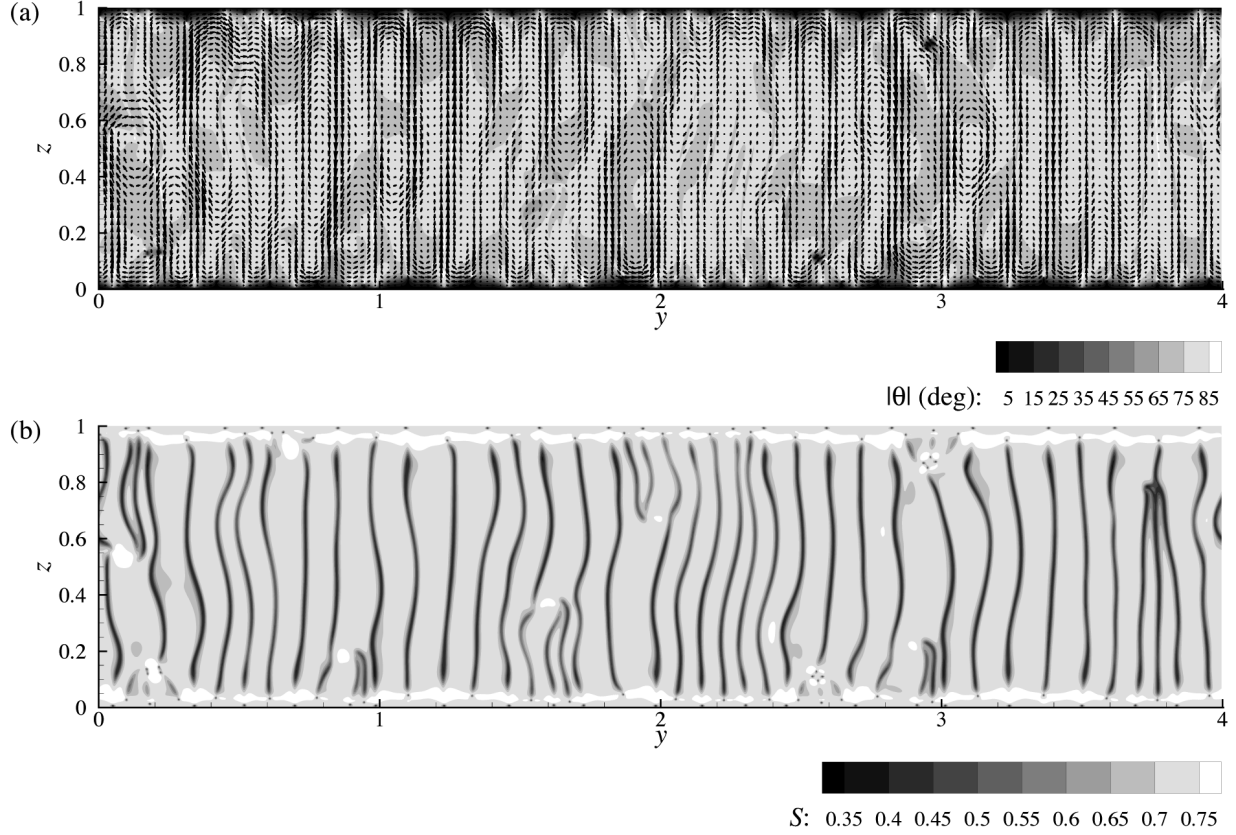


FIG. 14: (a) Secondary flow vector field (v_y, v_z) and tip angle magnitude $|\theta|$ scalar contour and (b) order parameter S scalar contour for $Er = 5000$ ($De = 5$) at $\tau = 28$ strain units. Note: a color animation showing the evolution of the flow and microstructure can be accessed by selecting the figure image.

perturbation in the secondary flow field in the vicinity of the $-1/2$ disclination, and increase in $\partial v_z / \partial z$ between the two defects as the $+1/2$ disclination moves upwards towards the center of the domain while the $-1/2$ disclination remains stationary at $(y, z) = (0.23, 0.71)$ [Fig. 13(c)].

For higher Er within this regime, although the first-observed defect structure is still that of $\pm 1/2$ defect pairs, forming near the upper and lower domain boundaries, the low-order cores from which the defects originate are not localized to small regions, but, rather, span the entire gap height between adjacent roll cells. This results in stationary $1/2$ -strength defects, of alternating sign, along the upper and lower domain boundaries. As was observed for lower Er values, upon formation of the $\pm 1/2$ pair of disclinations, the director orientation between the defects assumes an orientation that coincides with the flow axis. As a result, ridges, which extend across the entire

gap height, form between adjacent roll cells, wherein the tipping angle magnitude $|\theta|$ modulates between approximately 90 degrees at the ridge “peaks” and 75 degrees in the cores of roll cells along the y -direction. Given the relatively large De for these calculations, the director is subject to wagging with a frequency and amplitude that depends on the local orientation relative to the shear plane; the hydrodynamic torque imposed by the primary shear flow increases as the mean orientation tips away from the vorticity axis and approaches the shear plane. As the director undergoes wagging, 1-strength defects emanate from either end of the ridges as a result of the same *ridge-splitting* mechanism observed at much lower Er values. As was the case for lower Er within this regime, the locations from which disclinations originate and regions in which they reside following formation is in accordance with the findings of Larson and Mead¹¹. In Fig. 14, we show a snapshot of the secondary velocity, tip angle magnitude, and order parameter fields for $Er = 5000$ at $\tau = 28$ strain units, just following formation of the initial $\pm 1/2$ defects [as is evident from the small dark dots along the upper and lower bounds of the domain in Fig. 14 (b)] and prior to the formation of the first-observed ± 1 disclination pairs. Although many vortices have undergone splitting, the overall roll-cell structure initially remains intact [see Fig. 14 (a)]. The maximum secondary flow velocity, relative to the base flow, is 0.011, $|\theta|_{\max} = 90$ degrees, and $0.34 \leq S \leq 0.78$. The ridges from which ± 1 disclination pairs are continually produced coincide with the low-order bands, which (given that S drops from its equilibrium value of 0.74 to approximately 0.43) we referred to previously as cores, that span the height of the gap in Fig. 14 (b).

In Fig. 15, we present an example of the dynamics of the flow and director fields during the formation of the initial $\pm 1/2$ defect pair and subsequent production of the ± 1 defect pairs as the director between adjacent roll cells undergoes wagging. As is the case for all of our low to moderate shear rate calculations, the initial structure observed is that of roll cells and a modulation in the director field about the computational plane along the y -direction [Fig. 15 (a)]. The dark stripes

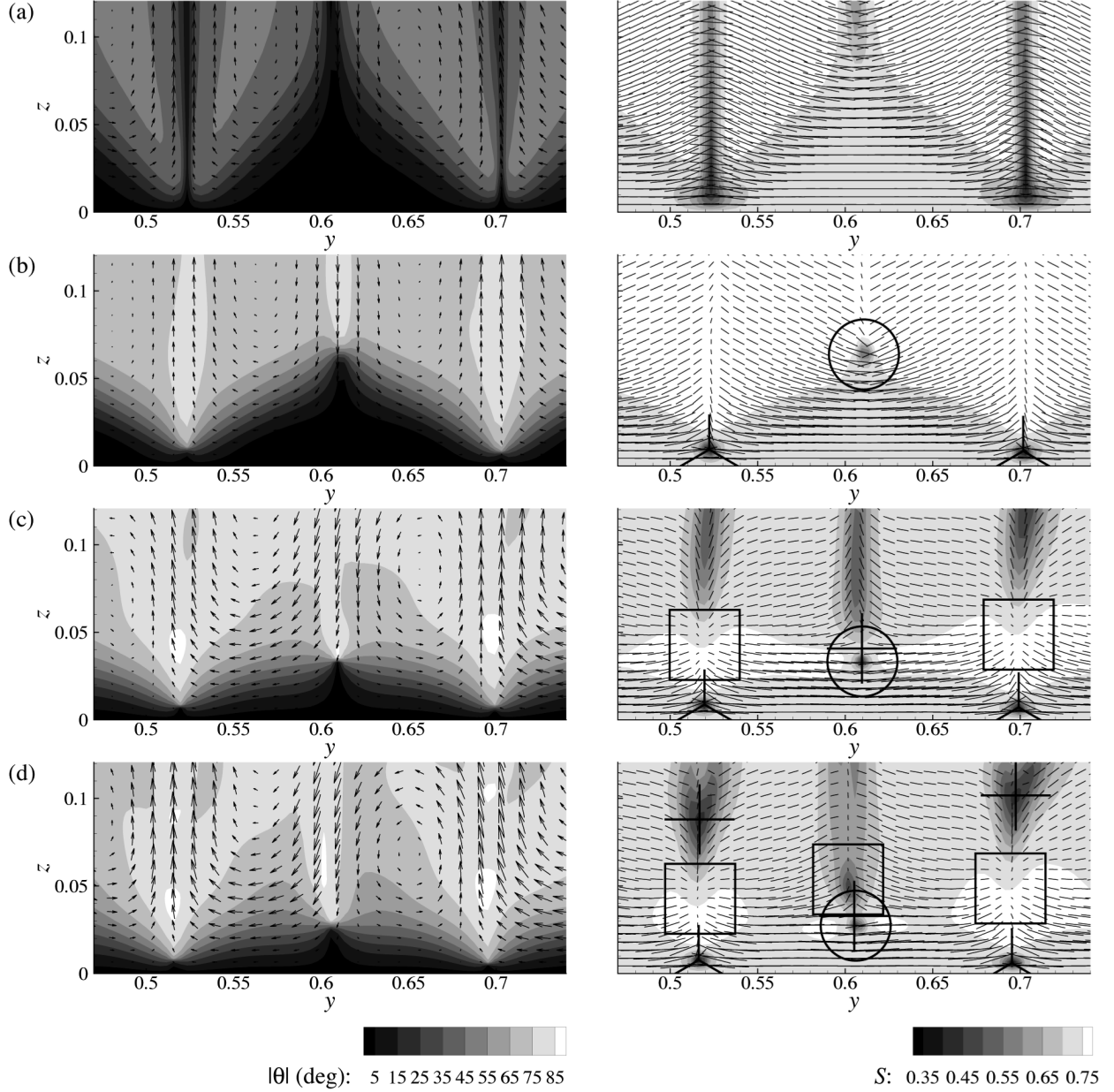


FIG. 15: Early-stage disclination formation for $Er = 5000$ ($De = 5$). (left) Secondary flow vector field (v_y, v_z) and tip angle magnitude $|\theta|$ scalar contour and (right) director vector field $\mathbf{d}(\mathbf{x})$ and order parameter S scalar contour at (a) $\tau = 9$, (b) $\tau = 16$, (c) $\tau = 27$, and (d) $\tau = 31$ strain units. The three-armed symbols and circles indicate the $+1/2$ and $-1/2$ disclinations, respectively. The crosses and squares indicate the $+1$ and -1 disclinations, respectively. Note: a color animation of the process depicted in this sequence of images can be accessed by selecting the figure image.

along $y = 0.53, 0.61$, and 0.70 in the order parameter contour in Fig. 14 (a) highlight the low-order cores that give rise to the formation of $\pm 1/2$ disclination pairs [Fig. 14 (b)] as ridges form between adjacent roll cells. As the director wags between the compression and extension quadrants of the

shear plane, ridge-splitting occurs at the ends of the ridge to create a ± 1 pairs of disclinations [Fig. 14 (c)]. As is indicated by the fact the subsequent ± 1 pair of disclinations in Fig. 14 (d) have low-order cores, ridge-splitting leads to low-order defect pairs when the director lies within the compression quadrant during the splitting process and the escaped configuration when the director is oriented within the extension quadrant. As ± 1 pairs of disclinations are continually generated between adjacent roll cells, defects annihilate via recombination in the compression regions [e.g., the ± 1 defect pair at $y \approx 0.6$ in Fig. 14 (d)], but remain somewhat stationary in the extension regions. This process continues, forming up to as many as four ± 1 disclination pairs propagating inward from the upper and lower domain boundaries, until the irregularity of the flow structure and polymer dynamics are such that there is little discernible structure within the domain.

B. High shear rates, $Er \gtrsim 10000$ ($De \gtrsim 10$)

As we continue to increase Er (and De), the initial roll-cell structure becomes increasingly transitory, and the irregular flow patterns and microstructure that develop give rise to a preponderance of the $1/2$ - and 1 -strength disclinations and eddies of decreasing sizes and strengths, characteristic of director turbulence^{41,42,43}. This refinement continues until, at $Er \approx 10000$ ($De \approx 10$), the solution exhibits neither disclinations nor roll cells. The system does, however, retain some structure along the span-wise direction that has the visual appearance of stripes. Specifically, there is a modulation in the mean orientation away from the shear plane (i.e., the x - y plane) along the vorticity axis; the angle between the director and shear plane is given as ϕ (not to be confused with θ , the angle between \mathbf{d} and the y - z plane). As an example of the striped texture observed at high shear rates, we present a snapshot of the secondary flow and banded structure associated with the modulation in the director field for $Er = 10000$ ($De = 10$) at $\tau = 35$ strain units in Fig. 16 (a), where the maximum secondary velocity magnitude is 0.009 and, away from the upper and lower

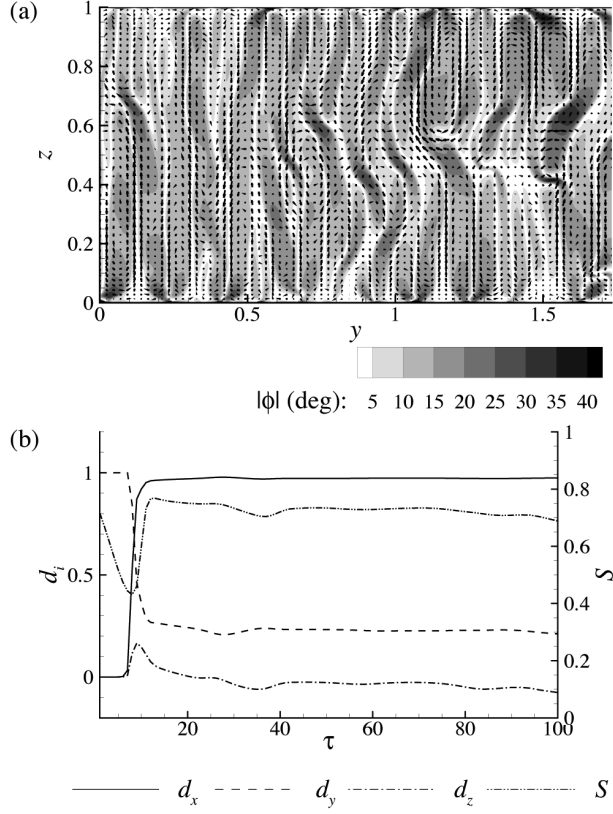


FIG. 16: (a) Secondary flow vector field (v_y, v_z) and tip angle magnitude $|\phi|$ scalar contour at $\tau = 35$ strain units and (b) director components d_i and order parameter S as a function of strain units τ at $(y, z) = (0.26, 0.25)$ for $Er = 10000$ ($De = 10$). Note: a color animation showing the evolution of the flow and tip angle can be accessed by selecting the figure image.

domain boundaries, $0 < |\phi| < 35$ degrees. This solution is representative of the quasi-stationary state (quasi-stationary in the sense that the general structure persists for the entire duration of our simulation, up to $\tau = 100$ strain units) reached at approximately $\tau = 25$ strain units. Although in regions in which the director orientation is almost parallel to the shear plane, as indicated by the white vertical bands in the $|\phi|$ contour in Fig. 16 (a), the director exhibits wagging, the director orientation remains relatively stationary in regions highlighted by dark vertical bands, where $|\theta| \gtrsim 5$ degrees, after the solution reaches (quasi-)steady state [cf. Fig. 16 (b)].

As we further increase Er (and De), although the span-wise length scale of the banded structure does not exhibit a dependence on Er , the amplitude of the modulation in ϕ decreases until, at $Er \approx 12000$ ($De \approx 12$), the director at each material point in the domain lies within the shear

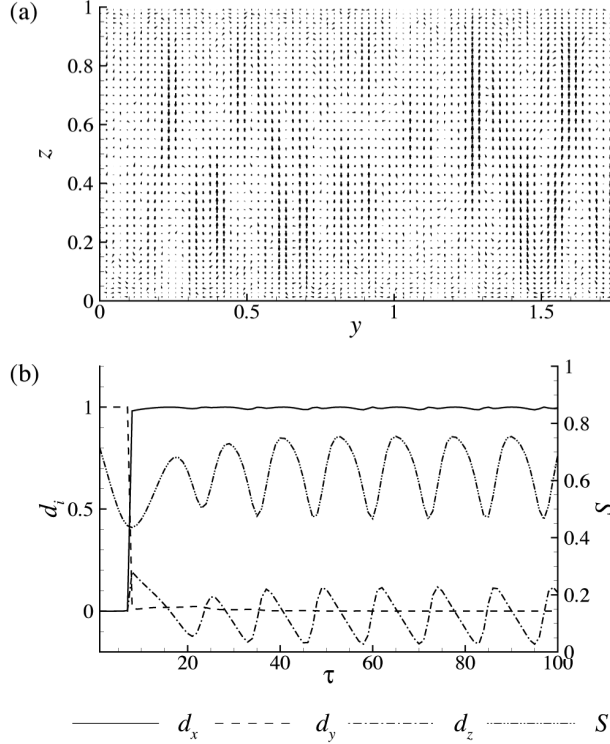


FIG. 17: (a) Secondary flow vector field (v_y, v_z) at $\tau = 35$ strain units and (b) director components d_i and order parameter S as a function of strain units τ at $(y, z) = (1.00, 0.50)$ for $Er = 12500$ ($De = 12.5$).

plane. Henceforth, we refer to this transition as the “shear-aligning” transition. In Fig. 17, we show an example of the secondary flow for $Er = 12500$ ($De = 12.5$) at $\tau = 35$ strain units, where the maximum secondary velocity magnitude is 0.002, and the evolution of the director components and order parameter at $(y, z) = (1.00, 0.50)$, an arbitrarily chosen point within the domain. We should note that the unapproximated Doi theory exhibits flow-aligning, where the director assumes a steady-state orientation along the flow axis, for De of this magnitude. As is highlighted by the dynamics of the the director and order parameter in Fig. 17 (b), the Bingham approximation simply predicts wagging, where the director oscillates about a fixed angle, with an amplitude that decreases monotonically with increasing De . This deficiency in the closure approximation used in our calculations does not, however, limit the model’s ability to capture the shear-aligning transition observed experimentally¹¹.

IV. DISCUSSION

As was stated in the introduction, although numerous experimental observations of the shear flow behavior of nematic liquid crystalline polymers, both lyotropic and thermotropic, have been reported in the literature, the observations most relevant to the results presented in this work are those of Larson and Mead^{10,11}. In these experimental works, Larson and Mead performed well-controlled analyses of the development of orientation and flow structure during shearing of solutions of the ‘model’ LCP poly(γ -benzyl-glutamate) (PBG) over a wide range of the Er - De parameter space. Their observations, both qualitative and quantitative, provide a basis from which we will evaluate the ability of the DMG to predict the shear flow behavior of nematic LCPs. Given that in the limiting case of $Er \rightarrow 0$, our results should compare well with those obtained using the LE theory, we will also make comparisons between our results and those of the relevant numerical works of Larson²⁴ and Feng et al.²⁵. As is commonly the case in the simulation of viscoelastic flows, these calculations present several challenges, positive-definiteness of \mathbf{A} and stability being the primary difficulties overcome in our investigations. We will, therefore, in concluding our discussion of the results, address the numerical challenges associated with this study.

A. Comparison with experiment and relevant numerical studies

Before discussing our results in the context of experimental observations, we briefly consider four relevant differences between the conditions in our simulations and those in the experiments referenced here. Firstly, we assume that there are no spatial gradients along the flow direction. Realistically, this assumption is only valid for two limiting cases: (1) low Er ($De \ll 1$), where the ratio between the stream-wise and span-wise length scales is very large (see, for example, Fig. 7 in [11]) and the system exhibits reasonable fore-aft symmetry along the flow direction;

and (2) shear rates for which $De \gtrsim 1$ ($Er \gg 1$), where the tumbling-to-wagging and subsequent wagging-to-flow aligning transitions coincide with the re-emergence of a banded pattern parallel to the flow direction. Secondly, the ratio between the Ericksen and Deborah numbers, which is a measure of the relative magnitudes of gradient elasticity and viscoelasticity, used in our calculations, $Er/De = 1000$, is approximately three orders of magnitude lower than the estimated value for the experimental systems. This choice of Er/De was primarily a consequence of computational limitations resulting from the fact that we considered Er (and De) values spanning nearly four decades and chose to hold the ratio Er/De fixed. Referencing the comment made at the end of Section II D, holding the ratio Er/De fixed allows us to make direct comparison between our results and those of experiment, where quantitative data reported by Larson and Mead¹¹ was collected over a range of shear rates for two different gap widths. But, given that we only vary Er in our calculations, the largest allowable value for Er/De is one for which the solution can be adequately resolved for the largest Er considered in this study ($Er = 15000$). Hence, $Er/De = 1000$ used in our simulations was determined using refinement studies. A possible consequence of using a relatively low Er/De is the inability to sufficiently separate the two distinct contributions to the polymeric stress, gradient elasticity, the driving force behind the Ericksen number cascade, and viscoelasticity, which stabilizes the system during the Deborah number cascade as the flow time scale becomes comparable to the relaxation time scale of the polymer, and, in turn, be unable to sufficiently resolve the two regimes.

The third relevant difference between the conditions in our simulations and those in the experiments referenced here is associated with the form of the nematic potential used in the DMG model. The form of the non-local contribution to the nematic potential used in our investigation neglects elastic anisotropy; i.e., the different modes of distortion, bend, splay, and twist, are each assumed to be energetically equivalent. It is generally believed that the twist energetic penalty is

much smaller than those of bend or splay, and that the bend and splay penalties are of comparable magnitude. In considering the effects of elastic anisotropy on the predictive capabilities of the LE theory, Tao and Feng⁴⁴ reported that reduction of the relative magnitude of the twist penalty did not bring about qualitative differences in their results; reduction of the twist penalty simply resulted in roll cell break-up and formation of ± 1 disclinations at lower Er . And lastly, the material constants for the PBG solutions used by Larson and Mead^{10,11} are not known. Using the weak-flow form of the polymeric stress¹⁶ and $\alpha_4/2$ as the characteristic viscosity, we determined the Leslie viscosities for our calculations to be $(\alpha_1, \alpha_2, \alpha_3, \alpha_5, \alpha_6) = (-10.8, -20.6, 0.765, 17.3, -2.58)$, which are of the order of those of the ‘typical nematic polymer’ used in Larson’s analysis of the LE theory²⁴ and the simulations of Feng et al.²⁵. It is, therefore, not surprising that the critical Er at which the perturbed system is unstable to roll cell formation, $Er \approx 40$, is comparable to those reported by Larson and Feng et al. As is evident by the qualitative and quantitative agreement between the DMG model predictions and the experimental observations reported by Larson and Mead discussed below, the differences in conditions between the two systems does not seem to inhibit the predictive capabilities of the DMG model.

Larson and Mead¹¹ characterize the Ericksen cascade as a series of instabilities that arise at low shear rates as a consequence of the competition between the viscous stress imposed by the flow and long-range gradient elasticity. In summary, a critical shear rate exists for which, after prolonged shearing, a banded texture appears in the form of birefringent stripes oriented along the flow direction; the banded texture undergoes refinement until reaching a steady-state spacing in 30-100 strain units, depending on the magnitude of Er and initial orientation; and disclinations having finite length, with a regularity in shape and intensity that diminishes with increasing Er , were found to usually reside between adjacent roll cells. Using polarizing microscopy, Larson and Mead found the banded texture to result from a periodic tipping of the mean orientation away

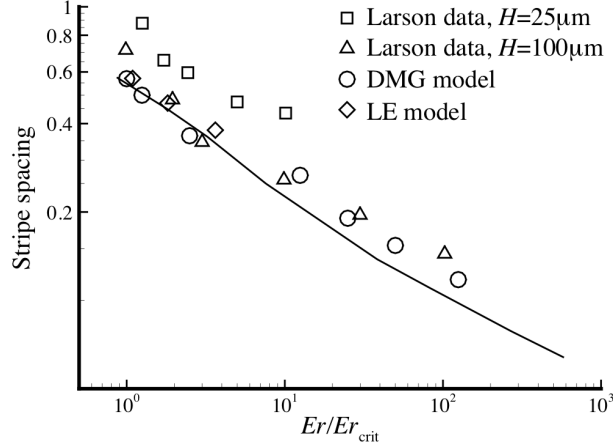


FIG. 18: Spacing of (strain-averaged) birefringent stripes, scaled by the gap width, versus scaled Er for the experimental observations of Larson and Mead¹¹, our DMG model results, and LE theory results reported by Feng et al.²⁵. The line represents the predictions of the linear stability analysis of the LE theory²⁴.

from the vorticity direction, into and out of the plane orthogonal to the flow direction (the y - z plane in our calculations). This is precisely the director field configuration predicted by both the DMG theory in our calculations and the LE theory in Larson's linear stability analysis²⁴, the earlier analysis of Manneville and Dubois-Violette³⁹, and the simulations performed by Feng et al.²⁵. Also in accordance with the LE model predictions, our DMG model results show that the periodic modulation in the director field is accompanied by the formation of stream-wise vortices (i.e., roll cells), and that, qualitatively, the refinement in the banded texture observed by Larson and Mead corresponds to a decrease in the roll-cell aspect ratio and corresponding increase in the tipping angle (referred to as θ in Section III) exhibited by the director.

Given the uncertainty of the material parameters for the PBG solutions used in the experimental systems and differences between those used in our calculations and those used in the LE calculations, quantitative comparisons between our data and those of Larson and Mead¹¹, Larson²⁴, and Feng et al.²⁵ will be based on the ratio Er/Er_{crit} , where Er_{crit} is the Ericksen value for which the perturbed system becomes unstable to the formation of roll cells. For quantitative comparison of the predicted steady-state band spacing, we calculate the birefringence pattern in

the same manner as was employed by Sgalari et al.¹⁴. In Fig. 18, we present the steady-state spacing of birefringence stripes, scaled by the gap width, as a function of the scaled Ericksen number Er/Er_{crit} for the experimental observations of Larson and Mead, our DMG model results, LE model results reported by Feng et al., and the prediction of Larson's LE theory stability analysis. For $Er/Er_{\text{crit}} \gtrsim 6$, where an irregular flow and orientation structure persists, band-spacing values are those associated with the dominant wavenumber of the birefringence pattern, as determined from the strain-averaged power spectrum generated using FFTs after the solution reached a quasi-stationary state. As is evident from the data presented in Fig. 18, there is good quantitative agreement between the steady-state band spacing predicted by the DMG model and the experimental values over a large range of Ericksen values. We should note, however, that the amount of strain required to reach steady state in our calculations was larger, by a factor of about 3, than the range of 30-100 strain units reported by Larson and Mead.

In considering the mechanisms by which disclinations form and the local orientation structure in the vicinity of disclination cores, due to the fact that there are no available experimental data that provide details of the microstructure at such small scales, we are limited to qualitative comparisons between predictions of the DMG model and experimental observations. Since the LE model, which neglects viscoelasticity, is intrinsically restricted from predicting the formation of $1/2$ -strength defects, comparison of our results to those of Feng et al.²⁵, in the context of the mechanisms of disclination formation, is limited to that of ± 1 disclinations. Given that the DMG model reduces to the LE model as $De \rightarrow 0$, it is not surprising that the ± 1 disclination pairs observed at relatively low Er form by the same ridge-splitting mechanism that was first identified by Feng et al.. Given the complexity that the solution exhibits for moderate to high Er , it is, however, somewhat surprising that this mechanism was universal throughout our calculations. With regard to the life span of ± 1 defects, there is also quantitative agreement between the predictions of the

DMG and LE models.

Although the $\pm 1/2$ disclination mechanism cannot be validated against available experimental or numerical data, a promising feature of the $1/2$ -strength defects observed in our calculations is their location. Larson and Mead¹¹ reported that defects usually originate and reside between adjacent roll cells. In accordance with Larson and Mead's observations, whether between daughter cells formed during the roll-cell splitting process ($Er \lesssim 1500$) or along the domain boundaries between adjacent roll cells ($1500 \lesssim Er \lesssim 6000$), $\pm 1/2$ were generally found to originate and reside between roll cells. For $Er \lesssim 1500$, there is an apparent discrepancy between the predictions of the DMG theory and the experimental observations of Larson and Mead for the case of ± 1 disclination pairs, in the sense that these form at the core of the roll cells instead of between them. However, for $1500 \lesssim Er \lesssim 6000$, 1 -strength defects were again found to originate between adjacent roll cells.

The Deborah number cascade is characterized by a series of transitions resulting from the dominant role of viscoelasticity that occurs when the time scale of the flow becomes comparable to, or larger than, the relaxation time scale of the polymer. In this regime, as De is increased, the system is stabilized by viscoelasticity and the texture refinement associated with gradient elasticity, which approaches length scales comparable to that of the molecular interaction length scale ℓ , subsides, leading again to the visual appearance of stripes oriented along the flow direction. As was verified by Larson and Mead using polarizing microscopy, the banded pattern results from modulations in the mean orientation away from the shear plane along the vorticity axis. Referencing the $De = 10$ ($Er = 1000$) results presented in Section III B, this is exactly the behavior predicted by the DMG model, wherein the solution contains neither roll cells nor disclinations and the director exhibits the afore mentioned modulation. We should note that, although the orientation structure was not investigated, similar high-shear-rate banded structures have been reported by Guido, Frallicciardi,

Grizzuti, and Marrucci⁴⁵, for aqueous solutions of HPC (hydroxypropylcellulose), and Tan and Berry¹³, for solutions of PPTA [poly(1,4-phenylene terephthalamide)]. Finally, as De is further increased, the flow-alignment transition leads to an apparent monodomain, where the mean orientation coincides with the flow axis throughout the domain. Although the Bingham approximation cannot capture the flow-aligning transition, this limitation does not seem to inhibit the model's ability to capture this transition in our calculations. While the mean orientation exhibits wagging, where the director oscillates about a fixed angle with an amplitude that decreases monotonically with increasing De , its dynamics are confined to the shear plane, and the result is, therefore, in qualitative agreement with the observations of Larson and Mead.

B. Numerical challenges

As is the case for viscoelastic flow calculations in general, two issues must be addressed when choosing an integration scheme: stability and preservation of the positive definiteness of the configuration tensor \mathbf{A} . In addition to concerns associated with numerical stability, which are defined in terms of the standard CFL constraints, where the maximum allowable time step is proportional to the minimum grid spacing or its square, in simulating the dynamics of polymeric fluids, the discretized form of the governing equations can become ill-posed if the accuracy of the method used cannot ensure that the positive definiteness of \mathbf{A} is maintained. Therefore, in surveying the literature, one finds this to be the leading topic addressed in simulating non-Newtonian flows. Given the complex (non-linear) form of the governing equation for the dynamics of \mathbf{A} (7), we have restricted ourselves to the use of an explicit integration scheme. In considering integration schemes, we found that the explicit Euler or standard second- and third-order Runge-Kutta methods⁴⁶ required the use of unreasonably small time steps [$\mathcal{O}(10^{-6})$ or smaller]. This constraint was alleviated by using the second-order Runge-Kutta TVD scheme proposed by Shu and Oscher³⁸,

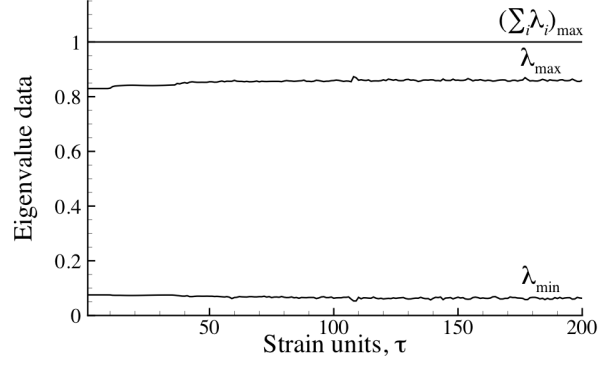


FIG. 19: Eigenvalue data versus strain units for $Er = 2000$ simulation.

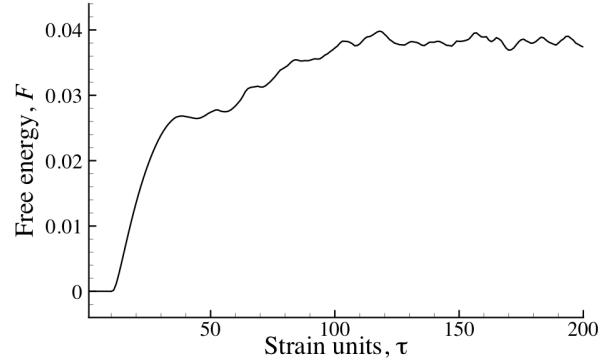


FIG. 20: Free energy eigenvalue data versus strain units for $Er = 2000$ simulation. The free energy F has been scaled by $\nu k_B T A$, where A is the dimensionless area of the computational domain.

which inherently limits the growth of grid-level oscillations. For the results presented in this work, $10^{-4} \leq \Delta t \leq 10^{-3}$. To highlight the fact that we maintain the positive-definiteness of \mathbf{A} , we show the strain evolution of the minimum and maximum eigenvalues of \mathbf{A} , λ_{\min} and λ_{\max} , respectively, and $|\sum_{i=1}^3 \lambda_i|_{\max}$ for our $Er = 2000$ calculation in Fig. 19. With regard to the eigenvalues, it is clear that they are all positive, and the sum $\sum_{i=1}^3 \lambda_i = 1$. The second-order tensor \mathbf{A} , which is symmetric, therefore, remains positive definite throughout the simulation.

The stability of the solution can also be monitored by considering the evolution of the system's free energy F , which, in the context of the DMG theory, can be written as

$$F = \int_A \nu \left[k_B T \langle \ln \psi(\mathbf{u}; \mathbf{r}) \rangle + \frac{1}{2} \langle V_{MG}(\mathbf{u}; \mathbf{r}) \rangle \right] dA, \quad (15)$$

where the domain area A is scaled by H^2 . For the Bingham approximation, $\psi(\mathbf{u}; \mathbf{r})$ takes the form

$$\psi_b(\mathbf{u}; \mathbf{r}) = \frac{1}{Z} \exp(\mathbf{u} \cdot \mathbf{T} \cdot \mathbf{u}), \quad (16)$$

where $Z = \int_{S^2} \exp(\mathbf{u} \cdot \mathbf{T} \cdot \mathbf{u}) d\mathbf{u}$ and the symmetric tensor \mathbf{T} is defined such that its eigenvectors and those of the second moment \mathbf{A} are co-aligned. The free energy, evaluated using the Bingham approximation and the nematic potential proposed by Marrucci and Greco, is therefore

$$F = \nu k_B T \int_A \left[\mathbf{T} : \mathbf{A} - \ln Z - \frac{3}{4} U \left(\mathbf{A} + \frac{\ell^2}{24} \nabla^2 \mathbf{A} \right) : \mathbf{A} \right] dA - F_0, \quad (17)$$

where F_0 is the equilibrium value of the free energy in the absence of flow and spatial gradients. Since the entropic contribution, $\mathbf{T} : \mathbf{A} - \ln Z$, cannot be expressed analytically in terms of \mathbf{A} , it is calculated using a fitting function generated in a manner similar to that used to calculate the components of the fourth moment \mathbf{Q} for the Bingham closure approximation³². In Fig. 20, we show the evolution of the non-dimensional free energy, where the free energy F is scaled by $\nu k_B T A$, for our $Er = 2000$ calculation. As a result of the imposed shear, the free energy increases monotonically until $\tau \approx 37$ strain units, when the formation of the first $\pm 1/2$ pair of disclinations alleviates stresses imposed by distortions in the director field. With increasing strain, the free energy continues to increase, exhibiting modulations as defects form and annihilate and the director field is continually perturbed, until a quasi-stationary state is reached at $\tau \approx 105$ strain units. Ultimately, it is bounded, further highlighting the fact that the solution remains accurate for the duration of the simulation. In conclusion, as an example of the complexity of the flow and microstructure that develops in our calculations, we show a snapshot of the secondary flow and director field for $Er = 2000$ at $\tau = 200$ strain units in Fig. 21.

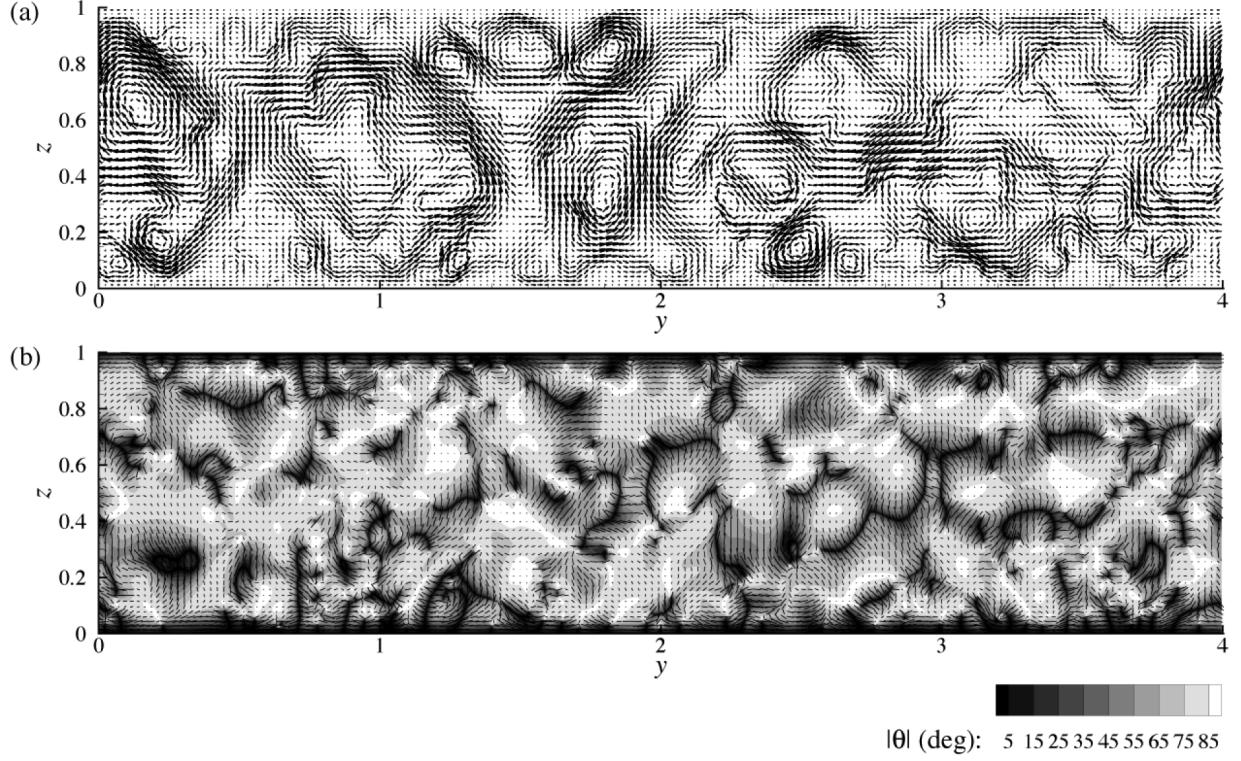


FIG. 21: (a) Secondary flow vector field (v_y, v_z) and (b) director vector field $\mathbf{d}(\mathbf{x})$ and tip angle magnitude $|\theta|$ at $\tau = 200$ strain units for $Er = 2000$.

V. CONCLUSION

For planar shear flow, the DMG model was found to exhibit dynamics in both qualitative and quantitative agreement with experimental observations reported in the literature for the so-called Ericksen number and Deborah number cascades. Within the Ericksen number cascade, where the dominant contribution to the stress is that of gradient elasticity, for increasing shear rates, the DMG model displayed four regimes: stable simple shear, stable roll cells, irregular structure followed by large-strain disclination formation, and irregular structure preceded by disclination formation. For increasing shear rates within the Deborah number cascade, where viscoelasticity is the dominant stress contribution, the DMG model exhibits two regimes: a stream-wise banded structure, in the absence of roll cells and disclinations, and shear-alignment, where the mean orientation lies within the shear plane throughout the domain.

Both 1- and $1/2$ -strength disclinations are predicted by the DMG model. The appearance of ± 1 disclinations is expected since these were observed in simulations of this flow using the LE model. Disclinations of strength $\pm 1/2$, however, have not previously been predicted in flow simulations, and thus may be seen as a major accomplishment for both the DMG model of LCPs and the computational procedures developed in this work. The mechanism by which each type of disclination formed was the same for the entire region of the $Er-De$ parameter space explored in our investigation. The formation of $\pm 1/2$ defects is a response of the system to an imposed curvature along either a localized region, as was observed in our low Er calculations, or de-localized regions such as the low-order regions between adjacent roll cells observed at moderate Er values. Similarly, ± 1 disclination pairs either formed from localized ridges, resulting in an escaped configuration, or emanating from the ends of large-scale ridges via the same *ridge-splitting* mechanism identified by Feng et al.²⁵ using the Leslie-Ericksen model.

Acknowledgments

The primary sources of funding for this work were the National Science Foundation (NSF), through IGERT grant DGE02-21715, and a grant to L. Gary Leal from the Unilever Corporation. The participation of Hector Ceniceros and Carlos García-Cervera in this project was supported, respectively, via grant DMS-0311911 and grants DMS-0411504 and DMS-0505738 from the NSF. The computations presented in this paper were carried out at UCSB on a Beowulf cluster purchased with funding from the aforementioned NSF IGERT grant in the Computer Science department and a Beowulf cluster in the Mathematics department purchased with funding from NSF SCREMS grant DMS-0112388.

* Electronic address: harley@engr.ucsb.edu

- ¹ S. Chandrasekhar, *Liquid Crystals* (Cambridge University Press, 1992), 2nd ed.
- ² P. G. de Gennes and J. Prost, *The physics of liquid crystals* (Oxford University Press, London, 1993), 2nd ed.
- ³ A. M. Donald and A. H. Windle, *Liquid crystalline polymers* (Cambridge University Press, 1992).
- ⁴ F. C. Frank, *Discussions of the Faraday Society* **25**, 19 (1958).
- ⁵ M. Reiner, *Physics Today* **17**, 62 (1964).
- ⁶ G. Kiss and R. S. Porter, *Molecular Crystals and Liquid Crystals* **60**, 267 (1980).
- ⁷ B. Ernst and P. Navard, *Macromolecules* **22**, 1419 (1989).
- ⁸ M. Srinivasarao and G. C. Berry, *Journal of Rheology* **35**, 379 (1991).
- ⁹ J. T. Gleeson, R. G. Larson, D. W. Mead, G. Kiss, and P. E. Cladis, *Liquid Crystals* **11**, 341 (1992).
- ¹⁰ R. G. Larson and D. W. Mead, *Liquid Crystals* **12**, 751 (1992).
- ¹¹ R. G. Larson and D. W. Mead, *Liquid Crystals* **15**, 151 (1993).
- ¹² J. Vermant, P. Moldenaers, S. J. Picken, and J. Mewis, *Journal of Non-Newtonian Fluid Mechanics* **53**, 1 (1994).
- ¹³ Z. Tan and G. C. Berry, *Journal of Rheology* **47**, 73 (2002).
- ¹⁴ G. Sgalari, L. G. Leal, and E. Meiburg, *Journal of Rheology* **47**, 1417 (2003).
- ¹⁵ G. Marrucci and F. Greco, *Molecular Crystals and Liquid Crystals* **206**, 17 (1991).
- ¹⁶ J. Feng, G. Sgalari, and L. G. Leal, *Journal of Rheology* **44**, 1085 (2000).
- ¹⁷ R. Zhou, M. G. Forest, and Q. Wang, *Multiscale Modeling and Simulation* **3**, 853 (2005).
- ¹⁸ G. Sgalari, L. G. Leal, and J. J. Feng, *Journal of Non-Newtonian Fluid Mechanics* **102**, 361 (2002).

- ¹⁹ R. Kupferman, M. N. Kawaguchi, and M. M. Denn, *Journal of Non-Newtonian Fluid Mechanics* **91**, 255 (2000).
- ²⁰ T. Tsuji and A. D. Rey, *Physical Review E* **62**, 8141 (2000).
- ²¹ T. Tsuji and A. D. Rey, *Physical Review E* **57**, 5609 (1998).
- ²² A. D. Rey and T. Tsuji, *Macromolecular Theory and Simulations* **7**, 623 (1998).
- ²³ T. Tsuji and A. D. Rey, *Journal of Non-Newtonian Fluid Mechanics* **73**, 127 (1997).
- ²⁴ R. G. Larson, *Journal of Rheology* **37**, 175 (1993).
- ²⁵ J. J. Feng, J. Tao, and L. G. Leal, *Journal of Fluid Mechanics* **449**, 179 (2001).
- ²⁶ M. Doi, *Journal of Polymer Science: Polymer Physics Edition* **19**, 229 (1981).
- ²⁷ M. Doi and S. F. Edwards, *The Theory of Polymer Dynamics* (Oxford University Press, 1986).
- ²⁸ R. B. Bird, C. F. Curtis, R. C. Armstrong, and O. Hassager, *Dynamics of polymeric fluids*, vol. 2: Kinetic theory (John Wiley and Sons, Inc., 1987), 2nd ed.
- ²⁹ W. Maier and A. Saupe, *Zeitschrift für Naturforschung Part A - Astrophysik Physik und Physikalische Chemie* **14**, 882 (1958).
- ³⁰ W. Maier and A. Saupe, *Zeitschrift für Naturforschung Part A - Astrophysik Physik und Physikalische Chemie* **15**, 288 (1960).
- ³¹ S. Prager, *Transactions of the Society of Rheology* **1**, 53 (1957).
- ³² C. V. Chaubal and L. G. Leal, *Journal of Rheology* **1**, 177 (1998).
- ³³ J. Feng, C. V. Chaubal, and L. G. Leal, *Journal of Rheology* **42**, 1095 (1998).
- ³⁴ J. Feng and L. G. Leal, *Physics of Fluids* **11**, 2821 (1999).
- ³⁵ M. Vinokur, *Journal of Computational Physics* **50**, 215 (1983).
- ³⁶ H. A. van der Vorst, *SIAM Journal on Scientific and Statistical Computing* **13**, 631 (1992).
- ³⁷ D. H. Klein, C. J. Garcia-Cervera, H. D. Ceniceros, and L. G. Leal, in *Proceedings of the 12th Computa-*

tional Techniques and Applications Conference CTAC-2004 (ANZIAM, 2005), vol. 46, pp. C210–C244.

- ³⁸ C. Shu and S. Osher, *Journal of Computational Physics* **77**, 439 (1988).
- ³⁹ P. Manneville and E. Dubois-Violette, *Journal of Physics* **37**, 285 (1976).
- ⁴⁰ P. Pieranski and E. Guyon, *Physical Review A* **94**, 404 (1974).
- ⁴¹ P. Manneville, *Molecular crystals and liquid crystals* **70**, 1501 (1981).
- ⁴² P. E. Claudis and S. Torza, in *Colloid and interface science*, edited by M. Kelker (Academic Press, Inc., New York, 1976), vol. 4, p. 487.
- ⁴³ P. E. Cladis and W. van Saarloos, *Solitons in Liquid Crystals* (Springer-Verlag, 1990), chap. Some non-linear problems in anisotropic liquids.
- ⁴⁴ J. Tao and J. J. Feng, *Journal of Rheology* **47**, 1051 (2003).
- ⁴⁵ S. Guido, P. Frallicciardi, N. Grizzuti, and G. Marrucci, *Rheologica Acta* **33**, 22 (1994).
- ⁴⁶ C. A. J. Fletcher, R. Glowinski, and M. Holt, eds., *Computational Techniques for Fluid Dynamics: Fundamental and General Techniques, Vol. 1* (Springer-Verlag, New York, 1991).